Bulletin of Volcanology (2025) 87:23
https://doi.org/10.1007/s00445-025-01799-z

FORUM CONTRIBUTION

Validation of 3D multiphase pyroclastic dilute current model: effects of confinement on the flows

Shungo Tonoyama[1] · **Takashi Nakamura**[1] · **Gert Lube**[2]

Received: 24 October 2024 / Accepted: 13 January 2025 / Published online: 28 February 2025
© International Association of Volcanology & Chemistry of the Earth's Interior 2025

Abstract

The volcanology community is systematically testing numerical models for pyroclastic density currents (PDCs) against datasets from that are defined through large-scale experiments. Here, we present the results of a three-dimensional Large Eddy Simulation (LES) mixture model for the case of a partially channel-confined, fully dilute, fully turbulent experimental PDC. Our LES model is based on solving the three-dimensional Navier–Stokes equations using a finite-difference method, the Constrained Interpolation Profile-Combined Unified Procedure (CIP-CUP) scheme. The model results are compared to the experimental dataset and to the results of a previous validation of a one-dimensional depth-averaged model. To better understand the effect of three-dimensionality of the flow and entrainment of ambient air on flow evolution, we contrast two scenarios: (1) a fully channel-confined simulation, limiting lateral entrainment of air; and (2) a partially confined simulation following the setup geometry of the experiment. For the first case, the modelling results are similar to those obtained in the depth-averaged simulation, with a close agreement of the position of the flow front against time but showing a more prominent head shape and body height than the physical experiment. In the second case, the front velocity is slightly overpredicted. However, the front height of the gravity current head, the body thickness, and the vertical velocity profiles closely mimic those measured experimentally. The downstream dilution of the PDCs is significantly enhanced in the partially confined scenario due to the formation of vortexes that laterally spill over the sidewalls, which is also observed in the large-scale experiment.

概要 (Japanese Abstract)
近年、火砕流 (PDC) の研究では大規模実験データにより提示されたベンチマーク問題を対象とし、コミュニティ主導でのモデルの検証が始まった。本研究ではPELEで行われた大規模実験でのデータを用い、混相流モデルの一つである三次元LES混合モデルの計算結果を報告する。本モデルは三次元Navier-Stokes方程式を有限差分法の一つであるCIP-CUP法で解いた乱流モデルである。計算結果は実験データ、既往の一次元浅水波方程式モデルと比較を行った。加えて、三次元性が流れに与える影響と連行 (エントレイメント) した周囲流体が流れの形成に与える影響を理解するため、側方での連行を制限し二次元計算の結果に近い閉じ込め条件 (confined condition) と、実際の実験設備に則し三次元性の考慮が可能な部分閉じ込め条件 (partially confined condition) の二つの流路を用意し検討した。Confined条件において、先端部位置は既往の浅水波方程式の結果と同様の値を示し実験結果を再現するものの、頭部は顕著に発達し、体部も実験より高い値を示す。一方でpartially confined条件では、流れの速度は実験結果よりも少し速いものの、頭部高さ、体部高さ、そして速度の鉛直プロファイルに関しては実験結果を良好に再現した。流路後半でのPDCの希釈は側方への流出による渦の崩壊に伴って促進され、これは大規模実験でも確認された。

Editorial responsibility: G. Valentine

✉ Shungo Tonoyama
shungo.tonoyama@riken.jp

[1] Department of Transdisciplinary Science and Engineering, Tokyo Institute of Technology, G5-3, 4259, Midori-Ku, Yokohama, Kanagawa 226-8502, Japan

[2] Volcanic Risk Solutions, Massey University, Private Bag 11 222, Palmerston North 4442, New Zealand

Keywords Pyroclastic density current · Multiphase flow · Mixture model · Entrainment · Confinement

Introduction

Pyroclastic density currents (PDCs), composed of volcanic gas, entrained air, and pyroclasts, are destructive gravity-driven flows that can have high velocities of 50 ~ 300 m/s (Fujinawa et al. 2008; Sparks et al. 1978) and high temperatures of 100 ~ 800 ℃ (Baxter et al. 2017; Auker et al. 2013). Due to the above hazardous characteristics, PDCs are a leading cause of fatalities from volcanic disasters, accounting for almost 30% of volcanic fatalities (Aucker et al. 2013). From a disaster mitigation perspective, accurate modelling of the internal structure of PDCs, as well as flow front velocity and gravity current height, is a key prerequisite to estimating flow inundation and hazard intensities. Furthermore, understanding spatiotemporal temperature changes due to mixing with ambient air could help estimate the severity of burn hazard impacts. However, modelling PDC has challenges that arise from the inherent uncertainty in the wide range of phenomena it encompasses (Lube et al. 2020). PDCs originate from various events, such as the collapse of lava domes and the fragmentation within eruption columns, resulting in significantly varying initial conditions. The difficulty in determining these initial conditions also makes comparison between numerical models and observations difficult.

To overcome the difficulties of in situ observation, lack of data on spatial–temporal changes in evolving PDCs, and the challenges in the physical modelling of PDC, community-driven efforts have been launched to compare numerical models with advanced experimental datasets. For concentrated PDCs, Roche et al. (2010) and Chedeville and Roche (2014, 2015) carried out a series of experiments to investigate the control factors of their run-out distance, such as fluidization and bed conditions. Breard et al. (2019a) assessed the kinetic theory of transient granular flows using a continuum multiphase model with two different granular-fluid rheologies. Gueugneau et al. (2021) presented synthetic benchmarking results for concentrated PDC using four commonly employed models. They also developed a new experimental facility called Pyroclastic Current Large-scale Apparatus using Synthetic Topographies (PyroCLAST) to deepen understanding of overbank flows from an experimental perspective (Gueugneau et al. 2022). The series of experiments demonstrated the relationship between slope angle, run-out distance, and the formation of overbank flows at a valley bend, which had been identified as a major cause for often unforeseen PDC avulsion into neighbouring valleys (Charbonnier and Gertisser 2008; Lube et al. 2011). Additionally, it is considered one of the benchmarks for future research.

Significant insights have been made from experimental studies regarding dilute PDCs as well. Andrews and Manga (e.g. Andrews and Manga 2011; Andrews 2014, 2019) conducted several experiments on dilute end-member regimes of PDCs. Heated particles are introduced into a chamber with visualization by laser sheet and video camera to investigate the influence of the topography with blocks, the turbulent state, and the entrainment process of PDC in two- and three-dimensional spaces. Dellino et al. (2007, 2010a, b) synthesized dilute PDCs following eruption column collapse in large-scale experiments. The multiphase flows of natural pyroclasts and gas were investigated to develop models for particle transport and for estimating dynamic pressure in PDCs (Dellino et al. 2010b), and to relate deposit characteristics to flow conditions (Dellino et al. 2019, 2020, 2021).

In this context, large-scale experiments on dilute PDCs have been conducted with the premise of providing datasets for benchmarking (intercomparison of numerical model results; Esposti Ongaro et al. 2020), leading to the sharing of numerous datasets for numerical simulations. Lube et al. (2015) obtained detailed time-series data focusing on the internal structure of the experimental currents using a large facility called Pyroclastic Flow Eruption Large-scale Experiments (PELE). Due to their fluid dynamics and thermodynamics scaling to natural PDCs, the large-scale experimental PDCs lend themselves to developing benchmark scenarios to test, validate, and improve numerical PDC models which previously relied on limited observational data. Motivated by this approach, a new community-based international benchmark exercise started. Within the pyroclastic model validation hierarchy of Esposti Ongaro et al. (2020), in the benchmark case, PELE's experiments provided datasets with well-defined initial and boundary conditions for consisting of a straight channel with partial confinement (Brosch and Lube (2020); Cerminara et al. 2021). Cerminara et al. (2021) processed data obtained by temporally and spatially averaging it, and with employing empirical approximations and statistical methods, to provide initial and boundary conditions tailored for different levels of complexity: transient two-, three-, and depth-average one-dimensional models, and stationary two-, three-, and depth-average one-dimensional models. Due to the inability to measure velocity, temperature, and volume fraction individually for each solid and gaseous fluid phase using particle image velocimetry (PIV) analysis and thermocouples, they assumed kinematic and thermal equilibrium between gas and particle in the flume. Initially, the experimental data were fitted with appropriate theoretical equations in space and time and then combined with the observed data. In cases where theoretical equations

were unavailable, various interpolations were employed. For instance, the velocity field was represented as the sum of mean and turbulent fluctuation velocities. In fitting velocity profiles obtained from PIV, the bottom layer was fitted with a classical empirical model for turbulence studies, while a Gaussian profile was used for the upper layer. When converting the obtained velocity field to time-averaged data, steady inlet conditions were also assumed.

These initial conditions, including the values in this study, are illustrated in Table 1. Shimizu et al. (2021) validated their depth-averaged two-layer model with this dataset for the two-dimensional model. In their research, the flow was modelled with dense and dilute concentration layers, and a one-way interaction was considered between layers. Detailed validation of the model's reproducibility using the experimental data enabled the quantitative investigation of the stratification process with a hindered settling model based on the simulated results. They demonstrated that the ratio of deposition speed at the base of concentrated flows to particle settling velocity at the bottom of dilute flows is crucial in determining the flow behaviour of PDCs, including the run-out distance.

We investigate the utility of the Large Eddy Simulation (LES) model in three-dimensional turbulent dilute PDCs under simplified initial conditions with confined/partially confined conditions. It has already been shown that simulations with the LES model for plumes (Cerminara et al. 2016) and PDCs (Esposti Ongaro et al. 2011) can adequately reproduce the dynamics of volcanic phenomena. However, a detailed comparison using experimental datasets and investigating the influence of confinement has not been conducted yet. We applied a three-dimensional mixture model on the basis of Ishimine (2005), which uses the LES model to evaluate the turbulence effect caused by confinement. We also assess the reproducibility of our model under spatiotemporal averaged input conditions.

Model description

General description

The main objective of this work is not to propose a novel modelling/scheme of PDC simulation but to examine how changes in the degree of lateral channel confinement influence the modelled flow using a three-dimensional LES scheme. In addition, we discuss how partial lateral confinement is taken into account and how air entrainment and boundary conditions in the model need to be adjusted. Because of these reasons, we applied an existing three-dimensional numerical PDC model (Ishimine 2005).

While a recent two-layer depth-averaged model (Shimizu et al. 2021) separated PDC into a suspended-load layer and a thin basal layer to model sedimentation with a hindered settling effect, calculating a thin basal layer, which has a thickness on the order of a few millimetres as obtained from PELE's experiments (Lube et al. 2015), is expected to pose challenges for a fully three-dimension model. Therefore, we employed a multiphase model with no particle–particle interaction and simple sedimentation. Regarding the turbulence model, a standard Smagorinsky term is employed.

Table 1 Input condition by Cerminara et al. 2021. In this study, we use time-averaged 1D, 2D/3D depth-averaged data

	Transient		Time-averaged	
	2D/3D	1D, 2D/3D	2D/3D	1D, 2D/3D
	depth-dependent	depth-averaged	depth-dependent	depth-averaged
Max. velocity $U(t)$ [m/s]	$6.378+1.267t-0.4550t^2-0.01049t^3$		6.451	
Max. velocity height $z_u\,(t)$ [m]	$0.2141+0.03276t$		0.2751	
wall exponent $\xi(t)$	$0.1662+0.04188e^{-2}t$		0.2374	
outer layer thickness $\chi(t)$	$4.294-0.3661t$		3.6	
Flow height		$z_u(t)(\chi(t)+1)$		1.265
$\overline{u}(z,t)$	$U(t)\left(\frac{z}{z_u(t)}\right)^{\xi}\exp\left[-\left(\frac{\frac{z}{z_u(t)}-1}{x}\right)^2-\xi\left(\frac{z}{z_u(t)}-1\right)\right]$		$U(t)\left(\frac{z}{z_u}\right)^{\xi}\exp\left[-\left(\frac{\frac{z}{z_u}-1}{x}\right)^2-\xi\left(\frac{z}{z_u}-1\right)\right]$	
$u'(t)$	$0.27\overline{u}$		$0.27\overline{u}$	
$u(t)$	$\overline{u}(z,t)+u'(t)$	$4.818+0.8469t-0.3160t^2-0.7049e^{-4}t^3$	$\overline{u}(z,t)+u'(t)$	4.8
Temperature T [K]	$303.9\,\exp\left(-0.0942\left(\frac{z}{z_u(t)}\right)^{1.71}\right)$		$303.9\,\exp\left(-0.0942\left(\frac{z}{z_u}\right)^{1.71}\right)$	292.29
Mass fraction ϕ_{mass} [K]	$0.876\,\exp\left(-0.0498\left(\frac{z}{z_u(t)}\right)^{1.74}\right)$		$0.876\,\exp\left(-0.0498\left(\frac{z}{z_u}\right)^{1.74}\right)$	0.4617

Governing equations

Our mixture model is based upon mass, momentum, and thermal energy conservation. All variables and input parameters are listed in Tables 1 and 2. We use a staggered mesh as the computational grid, and the flow velocity $\boldsymbol{u}$, pressure P, the density of the particle ρ_s, and the volume fraction of the particles ϕ_s are calculated based on the Constrained Interpolation Profile-Combined Unified Procedure (CIP-CUP) method that can solve a multiphase flow consisting of compressible and incompressible fluids (Yabe and Wang 1991). Since this method is a finite difference scheme with third-order spatial accuracy, it does not achieve exact conservation except in case of uniform velocity (Yabe et al. 2004). Hence, physical properties, density ρ_m, and molecular kinematic viscosity ν_m, of mixtures are estimated from weighted average value by ϕ_s.

$$\rho_m = \left(1-\phi_s\right)\rho_a + \phi_s\rho_s \tag{1}$$

$$\nu_m = \left(1-\phi_s\right)\nu_a + \phi_s\nu_s \tag{2}$$

The viscous coefficient ν is calculated from the sum of this molecular ν_m and turbulent viscosities ν_{SGS}. The details are described later.

The time progress of particle density, velocity, temperature, and pressure are applied to the following equations:

$$\frac{D\left(\phi_s\rho_s\right)}{Dt} = -\phi_s\rho_s(\nabla\cdot\boldsymbol{u}) - \nabla\cdot\left(\boldsymbol{\omega_s}\phi_s\rho_s\right) + \nabla\cdot(\nu\nabla)\left(\phi_s\rho_s\right) \tag{3}$$

$$\frac{D\boldsymbol{u}}{Dt} = -\frac{1}{\rho_m}(\nabla\cdot P) + \frac{\rho_m-\rho_a}{\rho_m}\boldsymbol{g} + \nabla\cdot(\nu\nabla)\boldsymbol{u} \tag{4}$$

$$\frac{DT}{Dt} = -\frac{P}{\overline{C}_v\rho_m}(\nabla\cdot\boldsymbol{u}) + \nabla\cdot(\nu\nabla)T \tag{5}$$

$$\frac{DP'}{Dt} = -\gamma^* P(\nabla\cdot\boldsymbol{u}) \tag{6}$$

$$\frac{D}{Dt} = \frac{\partial}{\partial t} + u\frac{\partial}{\partial x} + v\frac{\partial}{\partial y} + w\frac{\partial}{\partial z} \tag{7}$$

$$\rho_a = \frac{P}{RT} \tag{8}$$

$$\gamma^* = \frac{1}{1-\phi_s}\left(\frac{C_p}{C_v} - \frac{\phi_s\rho_s}{\rho_m}\frac{R}{\overline{C}_v}\right) \tag{9}$$

where $\boldsymbol{\omega_s}$ is settling velocity, $\boldsymbol{g}$ is the gravitational acceleration, P' is a deviation from the hydrostatic pressure, R is the gas constant, C_v, C_p, $\overline{C}_v$ are the specific heat at a constant

Table 2 All variables and their values in our model

Variables		Values
C_P	Specific heat at constant pressure of gas phase [J/(kg K)]	1.006×10^{3}
C_V	Specific heat at constant volume of gas phase [J/(kg K)]	7.170×10^{2}
C_s	Smagorinsky constant [-]	1.0
d_p	Diameter of particles [m]	33×10^{-6}
$\boldsymbol{g}$	Gravity force [m/s^2]	9.8
P	Pressure [Pa]	
R	Gas constant, [J/(kg K)]	287
T	Temperature [K]	
$\boldsymbol{u}$	Velocity [m/s]	
x_N	Nose position [m]	
α	Filter width [-]	1.0
γ^*	Modified ratio of specific heat of gas phase	
η	Dynamics viscosity of air [Pa•s]	2×10^{-6}
θ	Inclination of channel, [°]	6.0
ν	Kinetic viscosity of mixtures [m^2/s]	
ν_a	Kinetic viscosity of air [m^2/s]	1.49×10^{-5}
ν_s	Kinetic viscosity of particles [m^2/s]	4.0×10^{-2}
ν_{SGS}	SGS eddy viscosity [m^2/s]	
ρ_m	Density of mixtures [kg/m^3]	
ρ_a	Density of air [kg/m^3]	
ρ_s	Density of particles [kg/m^3]	2177
ϕ_s	Volume fraction of particles [m^2/s]	4.0×10^{-2}

pressure of gas-phase, a constant volume of gas-phase, and a constant volume of the gas-particle mixture, respectively. $\overline{C_v}$ is calculated by mass fraction as follows:

$$\overline{C_v} = \left(1 - \frac{\phi_s \rho_s}{\rho_m}\right) C_v + \frac{\phi_s \rho_s}{\rho_m} C_p \tag{10}$$

γ^* is the modified specific heat ratio. One feature of the above equations is that the continuity equation is not included explicitly (Ishimine 2005); however, it is restricted by the energy conservation of the gas-particle mixtures. As one feature of our model, we introduced the effect of settling, $-\nabla \cdot \left(\boldsymbol{\omega}_s \phi_s \rho_s\right)$ in Eq. (3). Ishimine (2005) considered the impact of settling to be negligible for sufficiently small particles (Kieffer 1984). However, in this study, we incorporated settling velocity, allowing for comparisons of sedimentations at the bottom of the flows. There are numerous studies on settling velocity modelling, and in this research, we used constant settling velocity based on the definition proposed by Kunii and Levenspiel (1969):

$$\boldsymbol{\omega}_s = \begin{cases} \dfrac{(\rho_s - \rho_a) g d_p^2}{18\eta} & \text{for } \mathrm{Re_p} < 0.4 \\ \left(\dfrac{4}{225} \dfrac{(\rho_s - \rho_a)^2 \boldsymbol{g}^2}{\rho_a \eta}\right)^{\frac{1}{3}} d_p & \text{for } 0.4 < \mathrm{Re_p} < 500 \\ \left(\dfrac{3.1(\rho_s - \rho_a) g d_p}{\rho_a}\right)^{\frac{1}{2}} & \text{for } 500 < \mathrm{Re_p} < 200{,}000 \end{cases} \tag{11}$$

where d_p is the diameter of the particle. The particle Reynolds number is $\mathrm{Re_p} (= d_p \rho_a \omega_s / \eta)$.

A suitable methodology for turbulence calculations is required to evaluate the effect of air entrainment on the volume fraction of particles and temperature. We applied a Smagorinsky model (Smagorinsky 1963) and assumed that only turbulent effects control their diffusions. Pressure change by turbulent mixing is assumed to be negligible.

The calculation of pressure at the new time step did not follow the well-known numerical model for ideal gas to avoid the numerical error from the equation of volume fraction (3) because of the relationship between the volume fraction of particles, bulk density, and pressure. The CIP-CUP scheme is introduced to calculate the pressure accurately (Yabe and Wang 1991). The CIP-CUP employs the time evolution equation for the pressure derived from the relationship between the time derivative of pressure, temperature, and specific volume (Ishimine 2005).

$$\frac{DP}{Dt} = \left(\frac{\partial P}{\partial T}\right)_V \frac{DT}{Dt} + \left(\frac{\partial P}{\partial V}\right)_T \frac{DV}{Dt} \tag{12}$$

In the CIP-CUP method, according to a time-splitting technique, Eqs. (3)–(8) are split into sequential solutions representing individual physical processes of advection, viscosity acceleration, pressure acceleration, and others such as temperature change due to compression. Similarly with a conventional Marker-and-Cell (MAC) method (Harlow and Welch 1965; Welch et al. 1965), physical processes that are not involved in pressure are first solved. Then, the spatial profile of pressure is solved with the Poisson equation derived from Eqs. (3) to (8). The Poisson equation includes a specific heat ratio γ^* as a parameter that indicates a reduction of compressibility due to the existence of solid components of pyroclasts. After pressure P is solved, in addition to the acceleration of flow velocity, the change of temperature caused by compression is calculated. When sufficiently hot PDCs entrain cold ambient air, gas-particle mixtures hardly decrease in volume due to differences in heat capacity, while the entrained air expands significantly. Comparing the volume of the air and PDCs immediately before entrainment with their volume after entrainment and heating, the latter shows an increase in volume, and the overall density of the flow decreases. This phenomenon is known to cause lift-off and affect the flow dynamics (Andrews 2014).

While advection terms are solved in a third-order spatial accuracy with a CIP scheme, temporal/spatial derivatives appearing in the governing equations are discretized in being based on a simple finite difference scheme such as a centre-difference approximation. Regarding temporal discretization, an explicit Euler scheme is employed except for a solution of pressure. Time increment Δt is determined every time step from the conditions for a stable solution. The Poisson equation for pressure P is solved by the Bi-CGSTAB method. See the references Ishimine (2005), and Yabe and Wang (1991).

The viscous coefficient v is obtained from the following equations.

$$v = v_m + v_{SGS} \tag{13}$$

$$v_{SGS} = \left(C_s f_s \Delta\right)^2 \sqrt{2 \overline{D}_{ij} \overline{D}_{ij}} \tag{14}$$

$$\overline{D}_{ij} = \frac{1}{2}\left(\frac{\partial \overline{u_i}}{\partial \overline{x_j}} + \frac{\partial \overline{u_j}}{\partial \overline{x_i}}\right) \tag{15}$$

$$f_s = 1 - \exp\left(-\frac{d^+}{25}\right) \tag{16}$$

where $\overline{D}_{ij}$ is the subgrid scale strain rate tensor, C_s is the Smagorinsky constant, and Δ is a filter width of LES. In the LES, while turbulent eddies that are larger than Δ are directly simulated, the influence of turbulent eddies that are smaller than Δ is modelled as turbulent viscosity v_{SGS}. To achieve the no-slip condition with the LES model, the Van Driest wall function, f_s, is applied around the wall with

Eq. (16) (Van Driest 1956). d^+ is non-dimensional distance and set to 10 in the present work. Generally, Δ is calculated based on the mesh-size Δ_{grid} used in our simulations.

$$\Delta = \alpha\Delta_{grid} = \alpha(\Delta x\Delta y\Delta z)^{\frac{1}{3}} \tag{17}$$

where Δx, Δy, and Δz, are mesh size in x, y, and z-directions, respectively, and α is the ratio of filter width to mesh size. While it has been recognized that the standard values of C_s are ranging between 0.1 and 0.2 (e.g. Deardorff 1970; Mason & Callen 1986; Germano et al. 1991), it is well known that the value of α should be appropriately adjusted depending on both modelling and discretization methods. In the present work, we use $\alpha = 1.0$, which is one of the common values in turbulence models (e.g. Germano et al. 1991; Shen & Yue 2001; Bini & Jones 2008).

Simulation conditions

Confinement conditions

As described in the previous section, the purpose of this study is to clarify the necessity of considering the shape of the experimental flume used in the benchmark problems based upon PELE data. The experiment itself is designed to be applied to several models at different levels of complexity (depth-average 1D model and 2D/3D model). However, the height of the channel sidewalls in the experiment is lower than the maximum flow depth, and videos of the experiment confirm the presence of overspill from the channel (Lube et al. 2015). In order to investigate the significance of this effect, we solved the flow with two types of channels that differ in the height of sidewalls: one is the confined setting, which has sufficiently high sidewalls of 4.0 m to prevent the overspilling and is close to the situation generally treated with a two-dimensional model, and the other is the partially confined setting, which follows the experimental setup (Fig. 1). Since the benchmark problem provides measured data at 2.65 m and 7.78 m in the downstream direction for the initial inflow, the computational domain was set to 9.8 m in the downstream direction and 4.0 m high, with a channel width of 0.5 m. Under partially confined conditions, a 0.3-m calculation area was added as a sidewall section. The partially confined setting follows the experimental setup and consists of three sidewalls at different heights, positioned at a distance of 0 to 3.28, 3.28 to 8.48, and 8.48 to 12.0 m from the upstream side with heights of 1.8, 1.2, and 0.6 m, respectively — and referred to as Sects. 1 to 3 in this study (Fig. 2a, c, e). Furthermore, the present study does not cover areas beyond the instrumented flume, such as the distal segments of the confined and unconfined outrun areas.

Initial and boundary conditions

At the upstream inlet boundary ($x = 0$ m), Cerminara et al. (2021) provided boundary conditions: time- and depth-averaged data on flow velocity, flow height, temperature and volume fraction of particles (Table 1). The end of the channel ($x = 12.0$ m) is set as the free (outflow) boundary, assuming that the spatial x-directional gradient of all physical quantities is 0. For the particle size, the experimentally determined depth- and time-averaged Sauter mean diameter $\left(d_p = 33\mu m\right)$ of the flow at the inlet boundary (Cerminara et al. 2021) was used in the simulations instead of the mean diameter $\left(d_p = 107\mu m\right)$. This approach is commonly adopted in the field of powder engineering with the aim of more accurately representing gas-particle drag and heat transfer for a size distribution than would be the case if standard mean diameters were used. In addition, Breard et al. (2019a, b) demonstrated the effect of particle

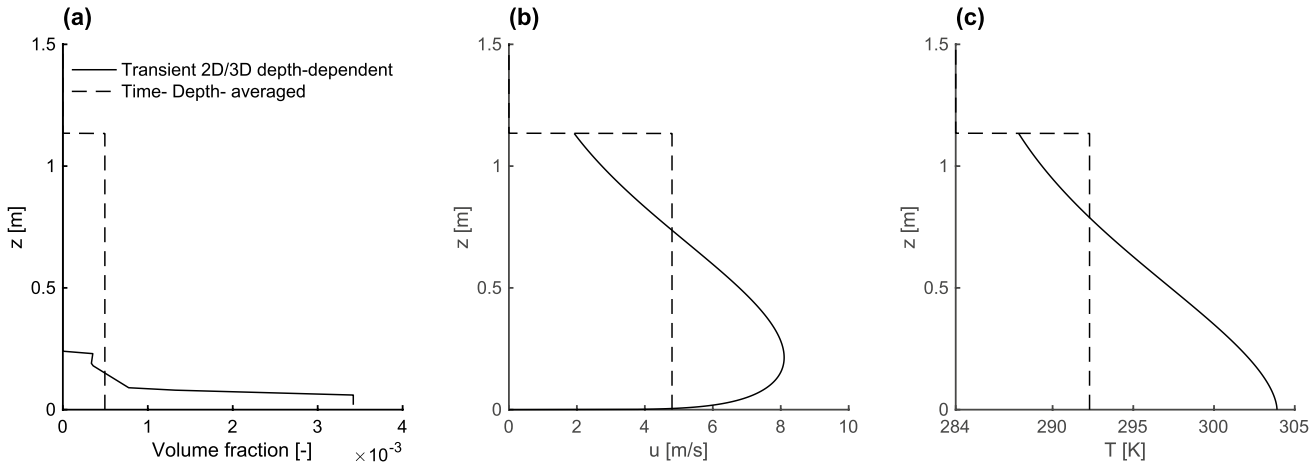

Fig. 1 Input conditions for volume fraction, horizontal velocity, and temperature. Solid lines indicate the experimental data at $t = 0$ s obtained by Cerminara et al. (2021), and dashed lines represent the time- and depth-averaged inflow conditions. In this study, we use time- and depth-averaged values

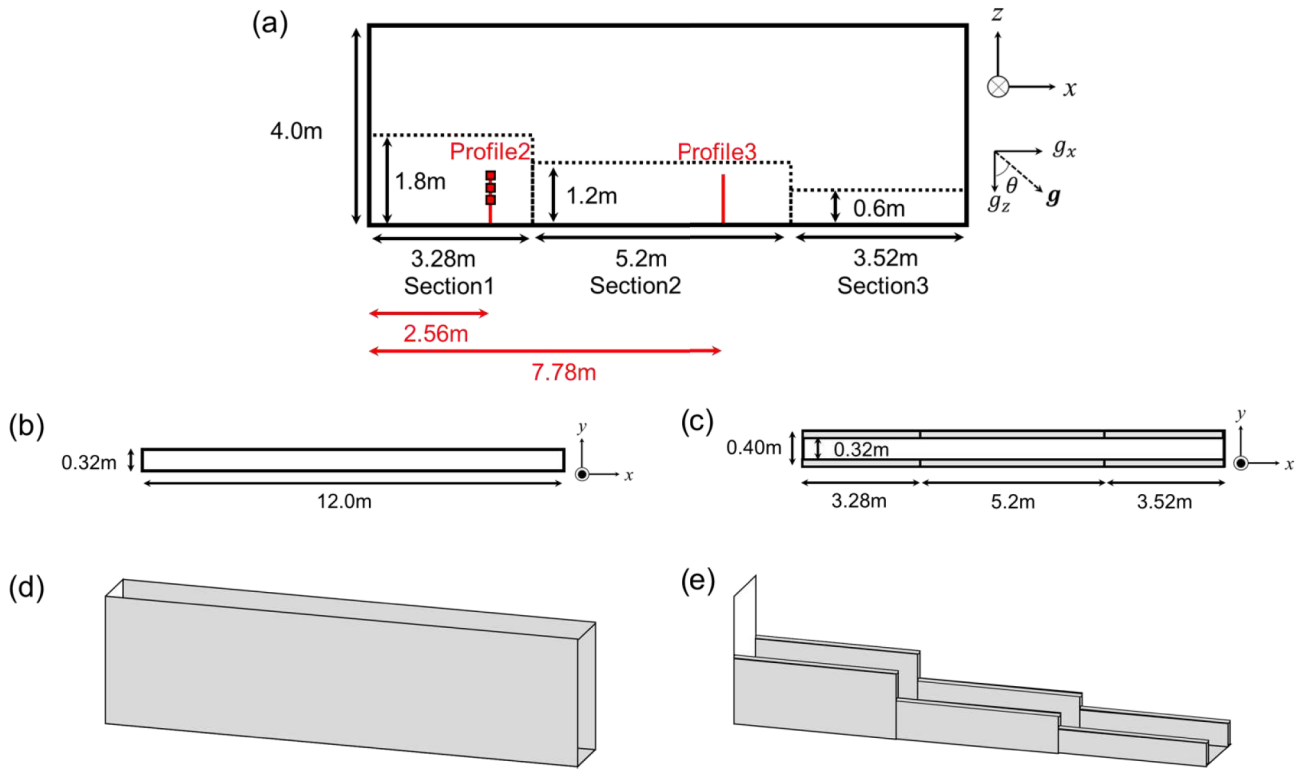

Fig. 2 The condition of confinement. **a** Side view of the calculation domain. The dashed lines show the height of lateral walls in the partially confinement setting, and the channel is divided into three sections according to the wall height: Sect. 1 ($x = 0$–3.28 m), Sect. 2 ($x = 3.28$–8.48 m), and Sect. 3 ($x = 8.48$–12.0 m). Red lines indicate the position of each profile where the experimental data was taken. **b** and **d** are upper and slant views of confined conditions, and **c** and **e** are upper and slant views of partially confined conditions, respectively. Gray colour represented the sidewalls

polydispersity on pressure diffusion and emphasizing the importance of Sauter mean in gas-particle flows such as PDCs. Note that, at the inflow boundary, the experimental flow is strongly vertically stratified with regard to particle volume fraction and grain size. Hence, a depth- and time-averaged value of the Sauter-mean diameter presents a strongly simplified boundary condition. In a follow-up paper, we intend to investigate the effect of particle size and polydispersity on flow behaviour. The bottom ($z = 0$ m) and side ($y = 0$, 0.32 m) in the wall setting are no-slip wall boundaries. The top ($z = 3.0$ m) and side ($y = 0$, 0.4 m) in the partially confined setting are a free boundary with constant pressure. The temperature and ambient pressure setting also follow the experimental conditions (Table 1), and the density of air is calculated from them.

Computational mesh

The computational domain is discretized with a Cartesian uniform mesh ($\Delta_{mesh} = \Delta x = \Delta y = \Delta z$). The mesh dependency was checked by comparing calculated results with those of different mesh sizes. The nose position of the pyroclastic flow was calculated and compared with Δ_{mesh} =2 and 4 cm (Supplementary Information S1). In this study, the front position is defined as the leading edge of the flow where the particle solids concentration is larger than $\phi_s = 1.0 \times 10^{-5}$. The results are generally in agreement, particularly reproducing flows in the early and late stages of the inflow. Based on these results, this study examined the influence of lateral confinement on the flows using the results of numerical calculations with a mesh size of 2.0 cm.

Results

Overview of the confined conditions

First we discuss the simulation results under the confined conditions. The schematic view of the transition process in Fig. 3 shows the definition of flow structures and the dilution process. The simulation results for the front position against time reproduce the experimental results well (Fig. 4). In the first 2 s, the coefficient of determination for the two-layer 1D depth-averaged model by Shimizu et al. (2021) and confined condition accounts for 0.99. Afterwards, a systematic departure from the experimental data begins to emerge, with an approximately 9.39% error appearing between them at $t = 2.5$ s. This means that the results of the numerical results, which did not take into account the actual confinement condition, quantitatively reproduce the experimental results.

We discuss flow regions based on the concentration ranges proposed by Breard and Lube (2017): the average volume concentration at the body is 7.4×10^{-4}, and the wake is 6.0×10^{-5}. Here, we set 5.0×10^{-5} as the boundary between the body and wake, 2×10^{-5} as the diluted region, and 1.0×10^{-5} as the concentration of the upper flow boundary. In the early stages of the influx of mixtures in Sect. 1 of the flume, the volume fraction of particles is uniformly distributed, and the head structure is generated at the front (Fig. 5, $t = 0.2$ s). Due to the spatial difference of velocity at the boundary between ambient air and PDCs, the flow entrains ambient air and reduces the volume fraction of particles as the head progresses.

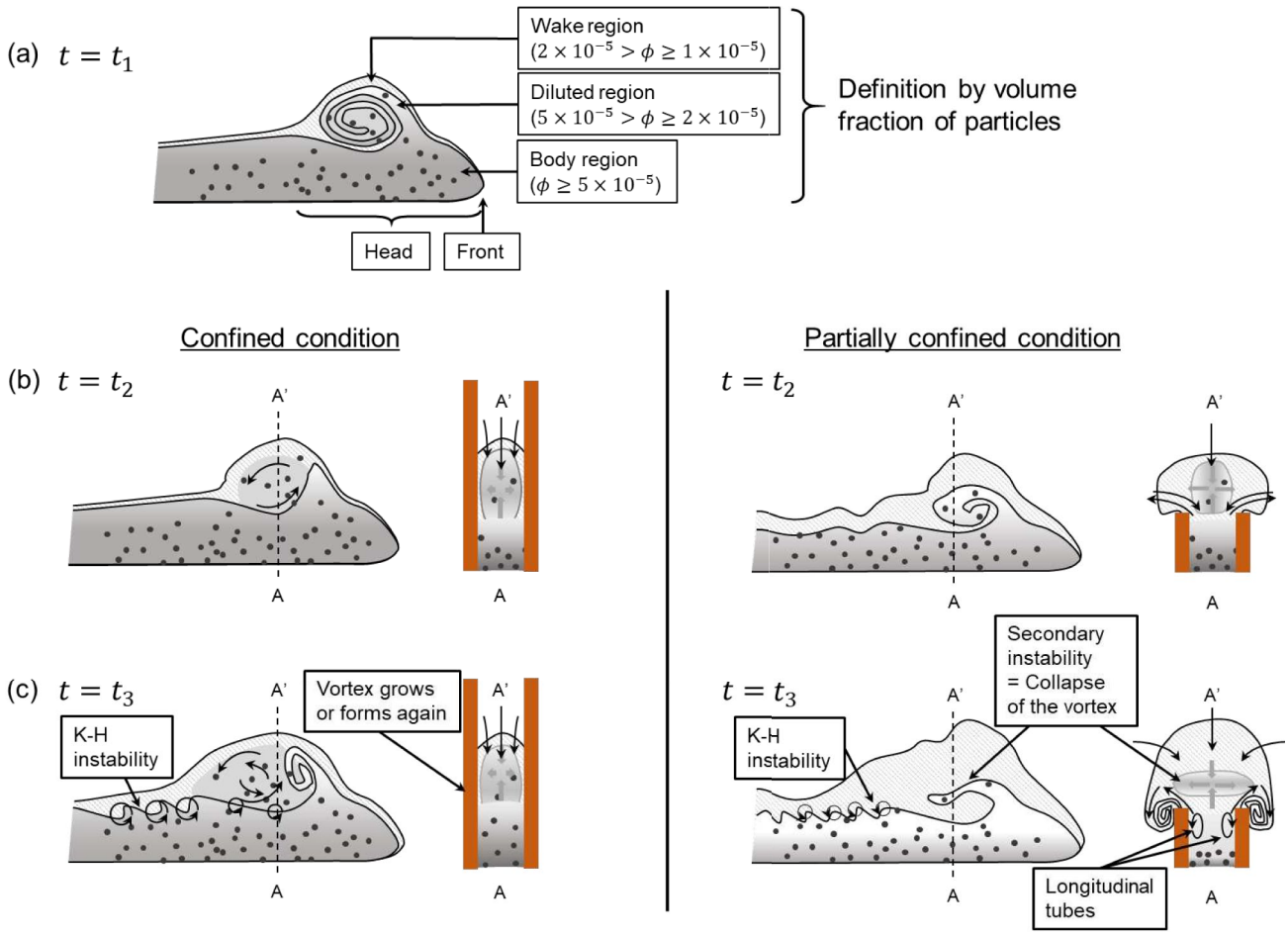

Fig. 3 Schematic of the progressing PDC in the present work. Entrained ambient air through the front inflates the head. The lateral outflow promotes secondary instability and mixing. Under confined conditions, the vortex, which is transported from the head, mixes at the surface of the body region and contributes to dilution. At this time, the head again forms a new vortex around its rear

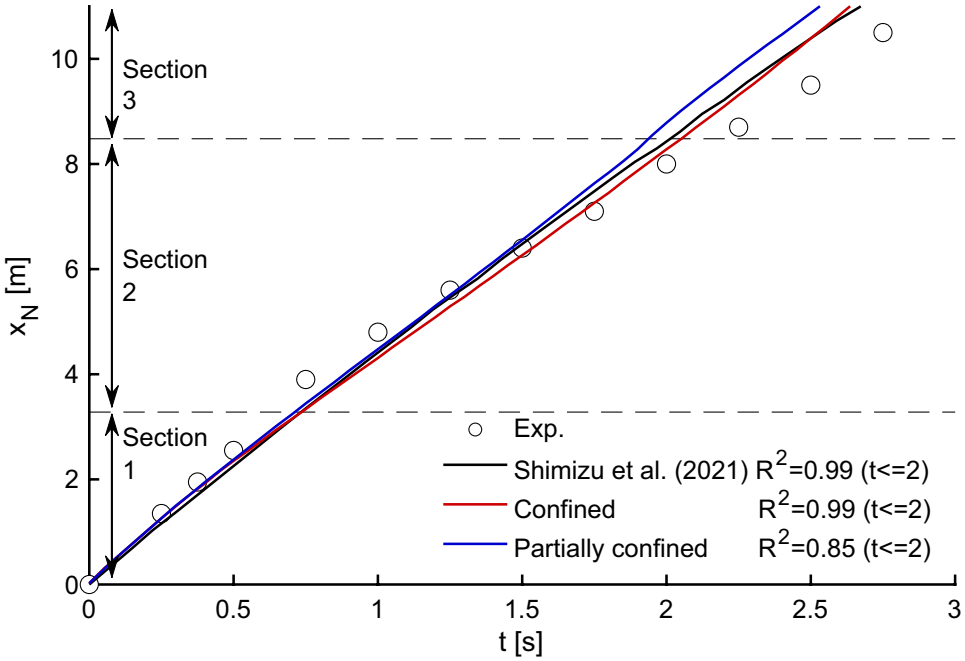

Fig. 4 Comparison of flow front position as a function of time for experimental results (circles) and simulation results (black line: previous results by the shallow water model (Shimizu et al. 2021), red line: confined setting, and blue line: partially confined setting). Dotted lines indicate divisions of each section of the flume. The results obtained by the confined condition, which does not account for lateral outflow, indicate outcomes similar to those of the shallow water model

Behind the progressing head, the flow of ambient air pushed away by the head generates an eddy. In the confined condition, because there is no lateral overflow and no restriction of flow height, clear and significant eddy formations are observed from the head to the rear. The volume fraction of particles at the centre of the vortex is around $\phi_s = 3.0 \times 10^{-4}$, which is ~ 60% of inflow conditions. After entering Sect. 2 (Fig. 5a, t = 2.0 s), the initial head vortex lags behind the progressing flow front, where new, smaller vortices begin to form, and the concentration at the centre is ~ 50% of initial values. Entering Sect. 3 (Fig. 5a, t = 3.0 s), the development of the head and the formation of a new vortex in the dilute region behind the head can be observed. A well-developed vortex mixes with the upper body region, and dilution proceeds. There is little difference in the flow height of the gravity current body region with time, and the height generally remains the same from the inlet to the head (Fig. 5a, t = 3.0 s). This feature of the height of a well-developed vortex ($1.5 \times 10^{-4} \leq \phi_s \leq 3.0 \times 10^{-4}$) at the head, and the absence of significant changes in inflow height at the body is similar to the results of the 1D depth-averaged simulations of Shimizu et al. (2021). Dilution continues behind the head, and a 1.5-m wake region was observed on 1 m of the body region (Fig. 5a, t = 4.0 s). Since there are no factors causing a sudden drop in flow velocities, several new vortices are formed from behind the flow due to the velocity difference between the ambient air and PDCs. These small to medium-sized vortices continue to grow, promoting further dilution. On the upper surface of the body region, wake structures ranging from 0.2 to 1.2 m in height form (Fig. 5a, t = 5.0 s).

Overview of the partially confined conditions

Partially confined conditions showed different flow behaviours. The front position in the partially confined condition accurately reproduced the experimental results during the initial phase (Fig. 4, $t = 1.5$ s). The flow structure is also very close to the result in the confined condition. The large vortex is generated behind the head, and the particle concentration at the centre of the vortex is around $\phi_s = 3.0 \times 10^{-4}$ (Fig. 5b and d, t = 1.0 s). Although there is a difference in that the rear of the vortex is significantly diluted ($\phi_s = 1.5 \times 10^{-4}$), the overall shape of the vortices remains largely the same. After this stage, differences appear between the confined and the partially confined conditions. The internal flow structure differs markedly from the cross-sectional data and shows different results. At $t = 2.0$ s, at a height above the channel sidewalls, the volume fraction decreased to less than 1.0×10^{-4}, which is almost 25% of the initial value, and the progressing head left this diluted flow region behind. This reduction in density and upstream transport in the wake is expected to be caused by overflow beyond the low sidewalls and lateral entrainment of ambient air. The volume fraction of the diluted flow region, which was left by the head behind it, becomes smaller, and the height of the body region also begins to decrease. We attribute this to the formation of Kelvin–Helmholtz (K-H) instabilities at the upper boundary of the body region towards the dilute region formed by the

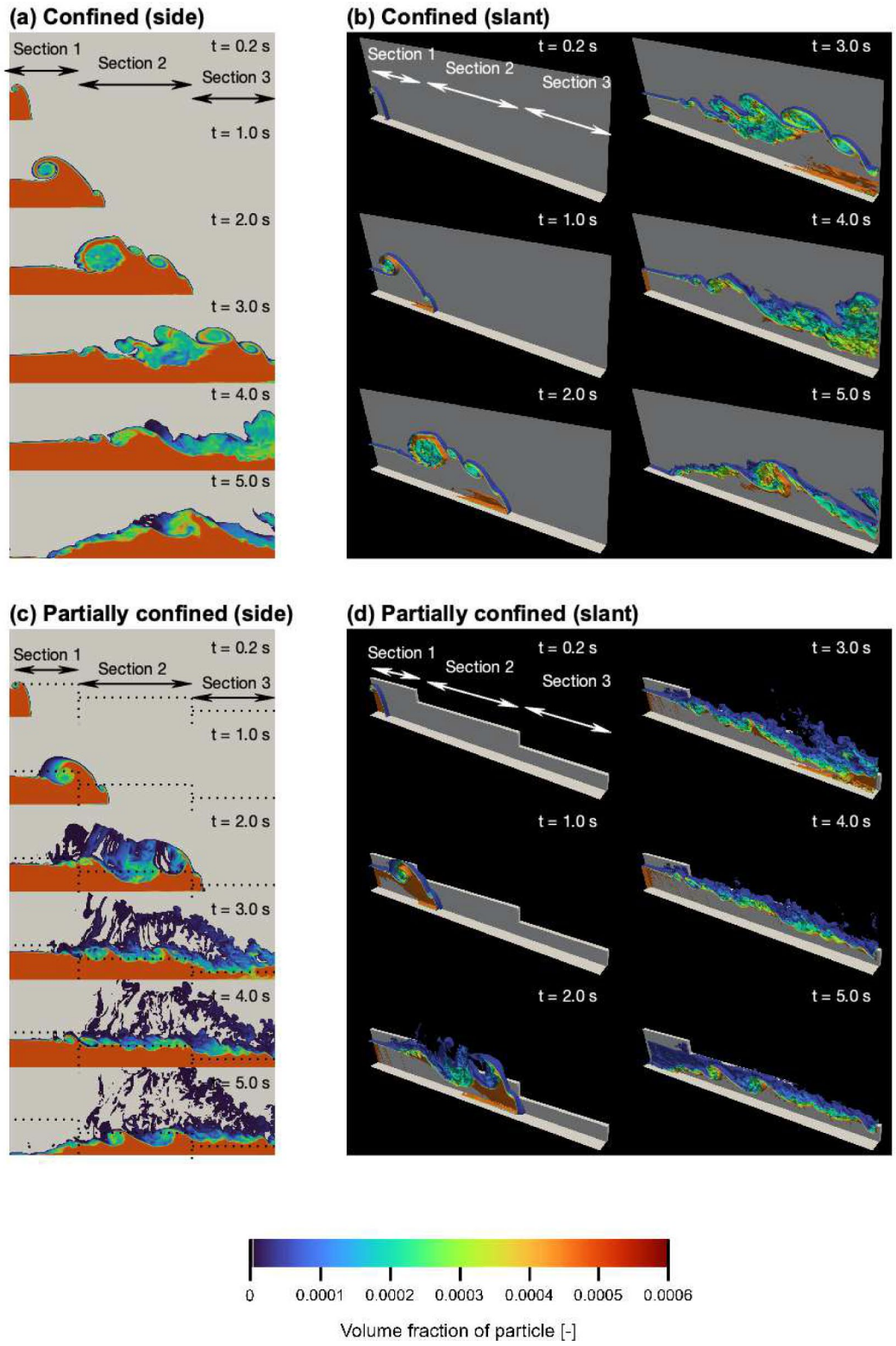

Fig. 5 Snapshots of side views (**a**, **b**) and slant views (**c**, **d**) under confined (**a**, **c**) and partially confined conditions (**b**, **d**). Colour scale represents the volume fraction of particles, and the contour plot express $\varphi\varsigma = 0.5, 1.0, 2.0, 3.0, 4.0, 4.5 \times 10^{-4}$. Black dotted lines in the side view of the channel setting and gray rectangles in slant view indicate wall structures

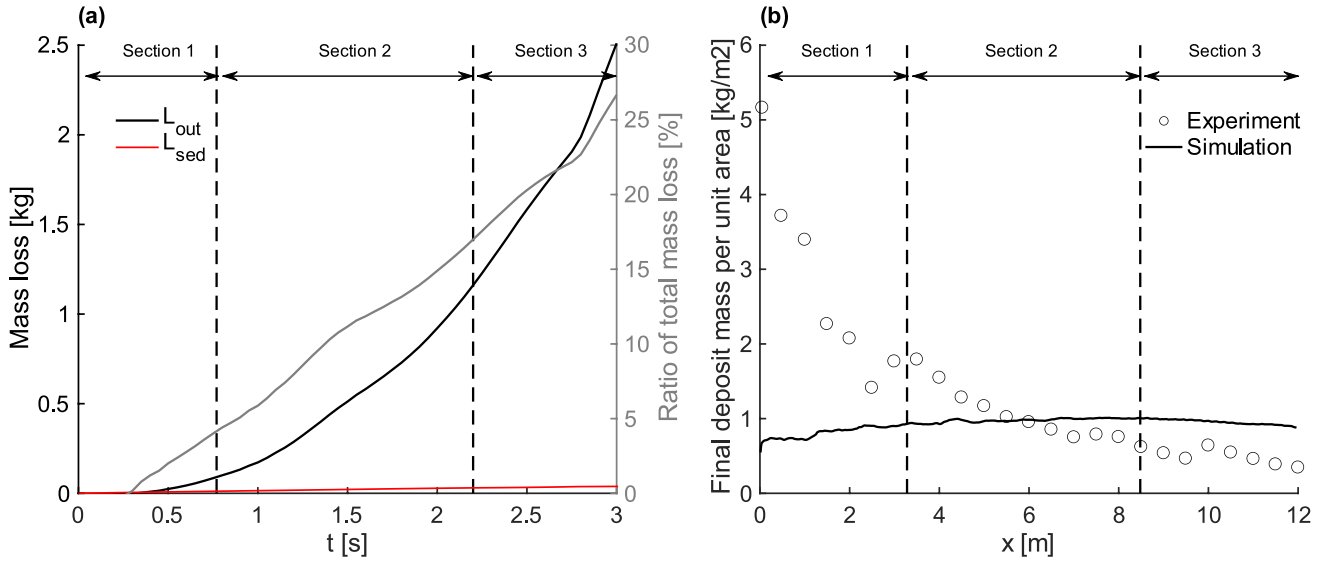

Fig. 6 **a** Mass loss by the outflow from the sidewall L_{out} and the sedimentation L_{sed} in the partially confined setting, and the ratio of total mass loss to total outflow mass. **b** Final deposit mass per unit area as a function of distance x. As the flow height exceeds that of the sidewalls ($t > 0.5$ s), the lateral outflow increases sharply

shedding of vortices at the rear of the head. In addition, in the partially confined condition, small vortices and vortex tubes are also generated in the vicinity of the head (Fig. 6b). This suggests that air transport takes place mainly from the front to the rear of the head and that the driving force is mainly the vortex in the x–z plane (Fig. 6d). As a result of this effect, the front position is overestimated by 14% at $t = 2.5$ s (Fig. 4). Entering Sect. 3 (Fig. 5, $t = 3.0$ s), the flow gradually entrains ambient air at the front and becomes more diluted under both confined and partially confined conditions; however, the diluted region and the degree of dilution are significantly different. In the partially confined condition, the height of the body region is equal to the height of the sidewall of the channel, and the upper diluted region behind the head is also predominantly diluted or detached from the body flow due to the mixing$\left(\phi_s \sim 1.0 \times 10^{-4}\right)$. A region with a reduction around 1.0×10^{-4} is clearly visible (Fig. 5d, t = 3.0 s).

There is mass loss over the sidewall in the partially confined setting. Mass loss by sedimentation L_{sed} and lateral outflow L_{out} are estimated from the following equations until the nose reaches the downstream boundary (Fig. 7). The integral is only applied inside the channel.

$$L_{sed} = \iint \omega_s \Delta t \left(\phi_s \rho_s\right) dxdy, L_{out} = \rho_s \int \phi_{xmin} u_{xmin} h_{xmin} dt - \int \phi(\boldsymbol{x}, t) dV - L_{sed} \tag{18}$$

By the time the front reaches the end of the computational domain, the mass that spilled over the channel reaches up to 25% of the inflow mass (Fig. 7). It is important to note the interpretation of the values here: the mass loss due to lateral outflow L_{out} represents the results calculated only for the first 3 s. This value is approximately ten times larger than the mass loss due to sedimentation L_{sed}. This discrepancy seems to be attributed to the absence of an initial stratification in this simulation, resulting in significantly higher values of volume fraction of particles and velocities in the upper region of the flows compared to the PELE's experiment (Fig. 1). As the flow develops, the presence of more regions with high velocity components and high particle concentrations that exist at heights above the sidewalls results in greater mass loss due to lateral outflow. In other words, the starting conditions of the simulation were non-stratified, which likely causes an overestimation of the fraction of mass that overflowed the channel. The mass transported and deposited laterally outside of the channel walls was not measured systematically in the experiment. Therefore, we could not evaluate this value. However, the results highlighting the effect of dilution due to three-dimensional considerations suggest the need for caution when selecting between two- and three-dimensional models in partially confined flow situations. This is because the processes of vortex formation and collapse, as well as the resulting dilution, differ between these cases (Fig. 6).

Moreover, in this model, the settling velocity is treated in a simplified method. While the upper layer can be represented by the settling velocities of Eq. 10 (Kunii and Levenspiel 1969), the bottom concentrated layer $\left(\phi_s \sim 0.01\right)$ exhibits complex physical processes such as deposition, erosion process, and clustering of particles (e.g. Girolami et al. 2010; Weit et al. 2018; Brosch and Lube 2020).

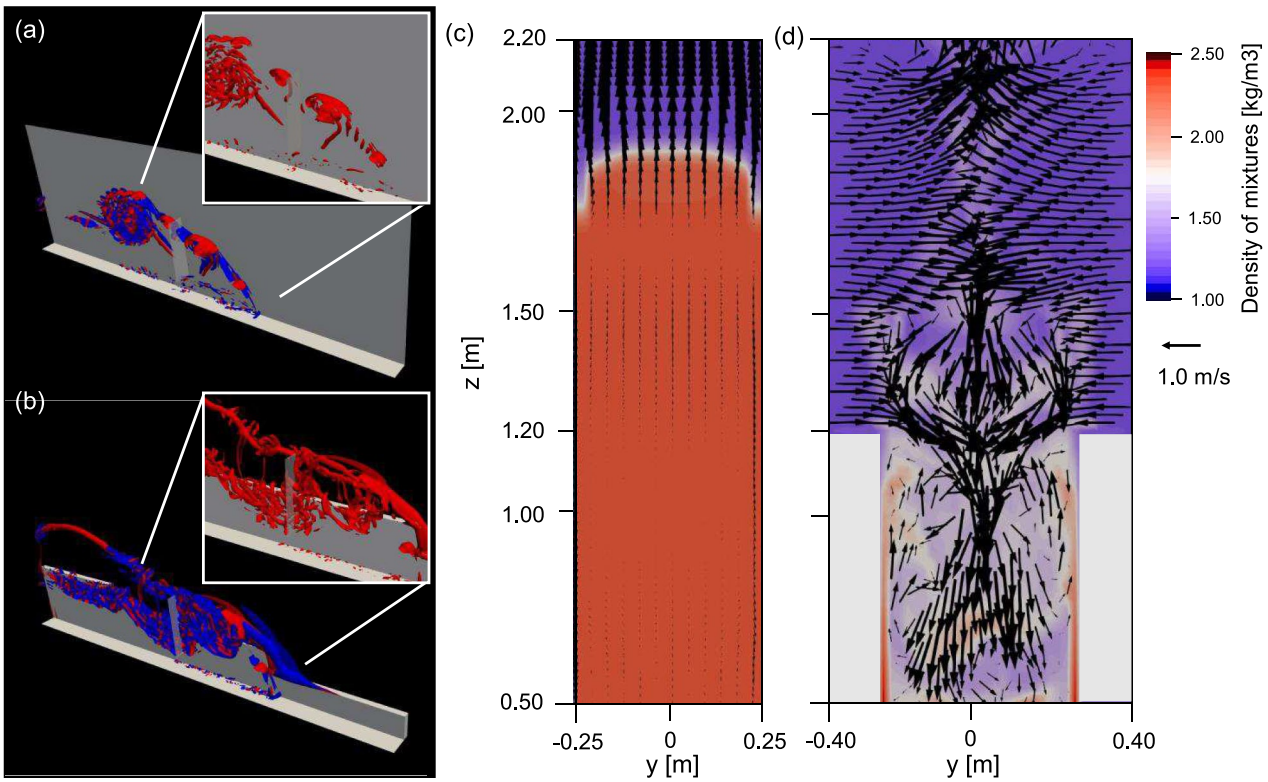

Fig. 7 **a, b** Second invariant of the velocity gradient tensor. At $t=2.0$ s. Red and blue contour colours represent +50 and −50 in confined and partially confined conditions, respectively. Upon closer inspection, longitudinal vortices that are not observed under confined conditions are clearly visible near the sidewalls under partially confined conditions. **c**, **d** Cross-sectional view at $x=6.0$ m. Colour scale indicated the density of mixtures and the black arrow showed the velocity vector. The black arrows indicate the magnitude of velocity

Furthermore, Shimizu et al. (2021) have demonstrated that the settling velocity can differ by two orders of magnitude between the bottom and upper layers. Therefore, future investigations with models that consider other physical processes are expected to elucidate the flow behaviour, such as run-out distance.

Turbulence structure

Many experimental studies have verified the three-dimensionality of the turbulence structure (e.g. Thorpe 1971, 1987, Caufield et al. 1996), and this also has been confirmed in numerical simulations (e.g. Caufield and Peltier 1994; Smyth 2006; Salehipour et al. 2016). The formation and growth of longitudinal vortices cause a large vortex to deform, break into smaller vortices, and eventually collapse. This process, known as the secondary instability, plays the role of a collapsing vortex during the transition process of the Kelvin–Helmholtz (K-H) instability. The observation of this secondary instability has been confirmed by performing three-dimensional calculations (Klaassen & Peltier 1985, 1991). Other studies have compared numerical and experimental results on the formation and deformation of eddies (e.g. Ashurst & Meiburg 1988; Martin & Meiburg 1991; Salehipour et al. 2016).

In our numerical results, significant dilution and the formation/dissipation of the vortex at the head can be considered a secondary instability. Ambient air entrained at the front formed the large vortex and promoted mixing at the head, apart from gradual dilution by K-H instability at the head (Fig. 4, $t=0\sim1.0$ s; Fig. 5a). In flume Sect. 1, the height of the flow exceeded the height of the sidewalls, resulting in lateral flows under the partially confined condition in addition to the vertical flow caused by mixing (Figs. 5b, 7a, c). This causes the secondary instability, and the rapid dilution creates large low and small medium concentration regions (Fig. 4a, c, $t=2.0\sim5.0$ s; Fig. 5c). On the other hand, under the confined condition, the flow velocity component in the y-direction is small, so the initially formed vortex separated and flowed backwards, forming a new vortex behind the head (Fig. 3b, c; Fig. 5b, d $t=2.0\sim5.0$ s; Fig. 7b, d).

Eddy structure in turbulent flows is generally visualized and investigated by the second invariant of the velocity gradient tensor Q (Fig. 7a, c). The second invariant is expressed

using the rate of strain tensor $\overline{D}_{ij}$ and the vorticity tensor $\overline{\Omega}_{ij}$ as follows:

$$Q = \frac{1}{2}\left(\overline{\Omega}_{ij}\overline{\Omega}_{ij} - \overline{D}_{ij}\overline{D}_{ij}\right) \tag{19}$$

In case the vorticity tensor is large enough ($Q > 0$), vortex development leads to gradual dilution. In contrast, in case the rate of strain tensor is more significant ($Q < 0$), shear is dominant. Figure 7 shows the positive ($Q = 50$) and negative ($Q = -50$) second invariants at $t = 2.0$ s for the two simulation results. In the confined conditions, positive regions are relatively common. The vortex developed behind the head, the internal vortex tube is larger than in the partially confined condition, and its elongation direction is relatively uniform. On the other hand, the partially confined condition has a more negative region except around sidewalls, and this indicates that shear dominates the flow. Around the edge of the sidewalls, there is the formation of small vortex tubes (Fig. 7b). The lateral flow exchange is thought to promote mixing, resulting in an expansion of regions with small volume fractions and a shrinkage of regions with intermediate volume fractions ($2 \times 10^{-4} \leq \phi_s \leq 4 \times 10^{-4}$). This observation could be interpreted as a stepwise dilution due to the rotating motion, with a larger intermediate volume fraction region ($\phi_s \sim 0.00025$) and a smaller wake region ($\phi_s \sim 0.0001$). Cross-sectional views (Fig. 7c, d) show that under partially confined conditions, inward flow is more pronounced near the sidewalls, and its influence extends into the centre of the flow ($z < 1.20$ m) and contributes significantly to the dilution of the internal concentration. The outward flow is more pronounced at the top of the flow, where flow exchange contributes to the formation of the wake area at the tail region (1.50 ~ 2.00 m). On the other hand, under confined conditions, there is little lateral or upward motion, and although moderate vorticity is observed near the vortex development height, a downward vertical current is formed as a whole. In the area of vortex development (1.00 ~ 1.50 m), dilution is occurring, but it is considered to be mixing due to vorticity rather than shear stress (Fig. 7a, b).

Body height

Next, results calculated with the confined/partially confined conditions were compared with experimental data. In the benchmark exercise, the body-wake boundary is not defined, for instance, by a threshold particle volume concentration.

The calculation results indicated that the two flow heads differ in their development, with the confined condition producing a well-developed head when profile 2 (Fig. 2a) is reached. In contrast, the partially confined condition results reproduced the dilution above the body and formation of the wake region (Fig. 8a, 0.5 ~ 1.5 s). Although slight dilution and a small area of the wake region are generated, there are no significant differences in the tail region at profile 2. The subsequent comparison in profile 3 (Fig. 2a) showed more clearly the difference in the confinement conditions. The confined condition shows a head height about 0.2 m higher than in the experiment and an overestimate of 0.3 ~ 1.0 m for the body. In contrast, under partially confined conditions, the transition time from the nose arrival to the head formation and body height agreed with the experimental results, except for the shape of the rear of the head (Fig. 8b, 1.0 ~ 3.0 s). One important observation here is that under confined conditions, the body height seems to be reproduced in profile 2, and the wake height appears to be reproduced in profile 3. However, the wake region is not well developed and the height difference between the body and wake is only ~ 0.05 m and there is no clear difference at this stage. Therefore, while the simplification of initial conditions may also have an impact, it is difficult to claim that the mixing process related to dilution is included. The results of the calculations suggest that the confined condition produces a higher overall body height and less fluctuations in the distal part of the body than the partially confined condition.

Wake height

The upper flow boundary is defined visually in the experiment as the interface between the particle-laden flow and the particle-free ambient air. In the numerical simulations, it is challenging to determine a strict interface, and we applied a threshold value of the volumetric particle fraction, $\phi_s = 2 \times 10^{-5}$ (Fig. 5a). The 4-m-high sidewalls, higher than those used in the experiment, caused shear between the sidewalls and the flow at heights where it would not have occurred under normal conditions. However, while dilution is promoted, the concentration decreased by only about a factor of 2, and there was little difference in height between the body and the wake (Fig. 8a, b). In the partially confined condition, on the other hand, the density profiles are different despite similar cross-sections due to dilution caused by the secondary instability. The wake height and body height are distinctly different, and the area occupied by the dilute region is large. As shown in Fig. 4, some of this dilute part is completely detached from the flow, but this is not a positively buoyant lift-off as generally described in the end state of PDCs. The results show that the wake heights in the confined conditions reproduce the experimental results well, especially in profile 3, where the results are far apart in the partially confined conditions (Fig. 8). One possible cause is the model limitation in this study. As this study employs a space–time averaged inflow of homogenous fluid with only a single particle size, it does not consider particle interactions (e.g. collision, cohesion) or segregation processes. Moreover, in the LES model, differences attributable to the

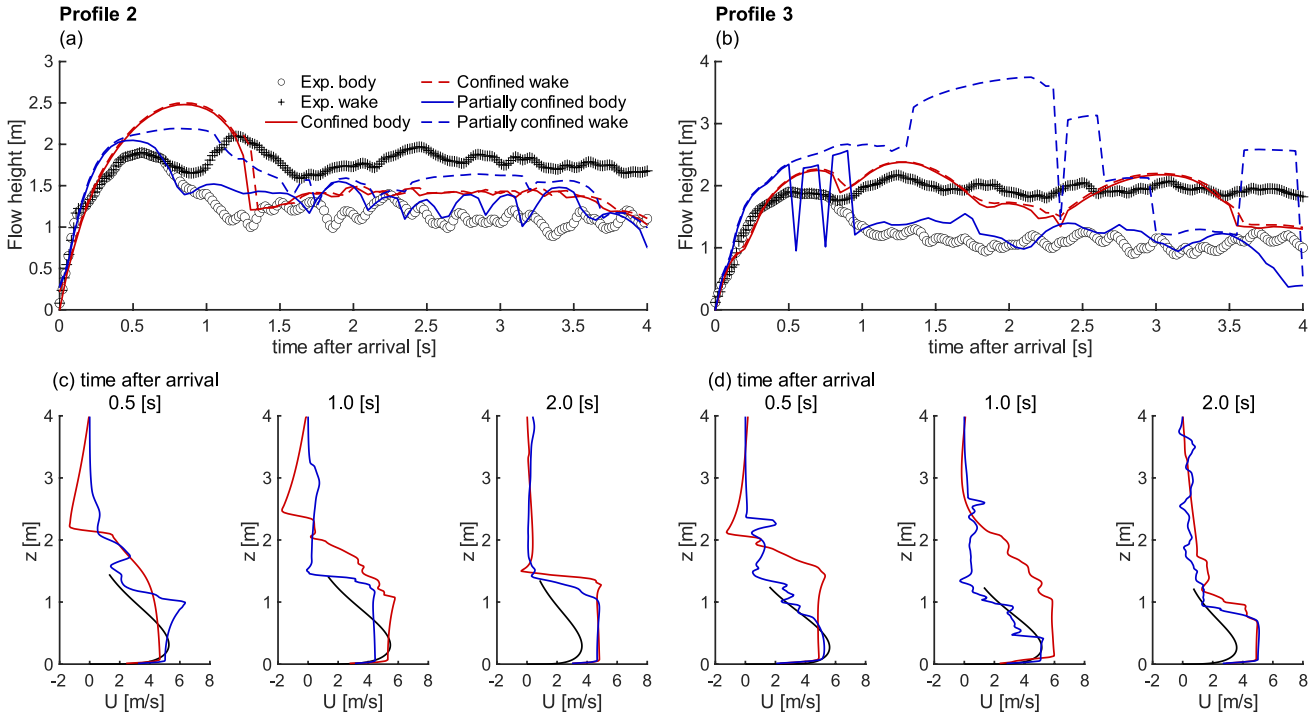

Fig. 8 **a**, **b** Body and wake height comparisons under the confined (red) and partially confined (blue) conditions at each profile ($x = 2.56$, $y = 7.78$ m). Black circle and cross represent experimental data of body and wake height, respectively. Each line style corresponds to simulation results of body and wake height. **c**, **d** Vertical profile of horizontal velocity at three time steps: 0.5, 1.0, and 2.0 s. Black lines are experimental observation data; red lines are confined conditions; blue lines are partially confined conditions

microstructure of turbulence are also not taken into account. Therefore, the common filter width may overestimate the entrainment rate and the volume of the ash cloud surge, and it is necessary to investigate the dependence of other mean diameters and polydispersity in the follow-up studies.

Flow velocity

We now focus on the conditions inside the flow and the comparison of velocity profiles at multiple locations (Fig. 9). In the present study, we compare the time variation of velocity in the x- and z-directions at $z = 0.42$, 0.72, and 1.07 m in profile 2 with the experimental results. The velocity in the y-direction (v, perpendicular to the side walls) is presented but not compared with data because it is not measured in the experiment. For the horizontal velocity, u, the experimental results show small turbulence fluctuations below $z = 0.72$ m. This result is consistent with the general tendency of PDC in the upper body and wake region, except for the lowermost region of the body, where the concentration of particles is high. At the same time, larger heights are characterized by significant fluctuations and increased flow complexity. The numerical results under confined conditions (red line in Fig. 9) show relatively small changes in flow velocity over time, and its value is generally close to the maximum values of u in experimental results. The partially confined condition (blue line in Fig. 9) reproduced the fluctuation in horizontal velocity, especially at $z = 1.07$ m, the highest point in this study, in which turbulent components become stronger (Fig. 9a). For the velocity components in the z-direction (w; Fig. 9b), comparison of simulation results across all three locations indicated that under confined conditions, there was a small vertical variation for most time intervals and averaged ~ 0 m/s, while under partially confined conditions, downward velocity was predominant and fluctuated. In comparing the two velocity components with experimental data, at $z = 1.07$ m, the partially confined conditions exhibited more significant variability in velocity fields compared to the confined conditions. Under partially confined conditions, the amplitude of the fluctuation is approximately twice that observed in the experiment, at around 1 m/s, but the maximum velocity is the same at ~ 1.5 m/s ($t > 0.5$ s). Additionally, the vertical profile at each time step in profiles 2 and 3 (Fig. 8c, d) suggests that the confinement affected the reduction in horizontal velocity and partially confined condition reproduced experimental results for about 1.0 s after reaching profile 3 very well (Fig. 8d). When comparing the body height at profile 3, the confined condition

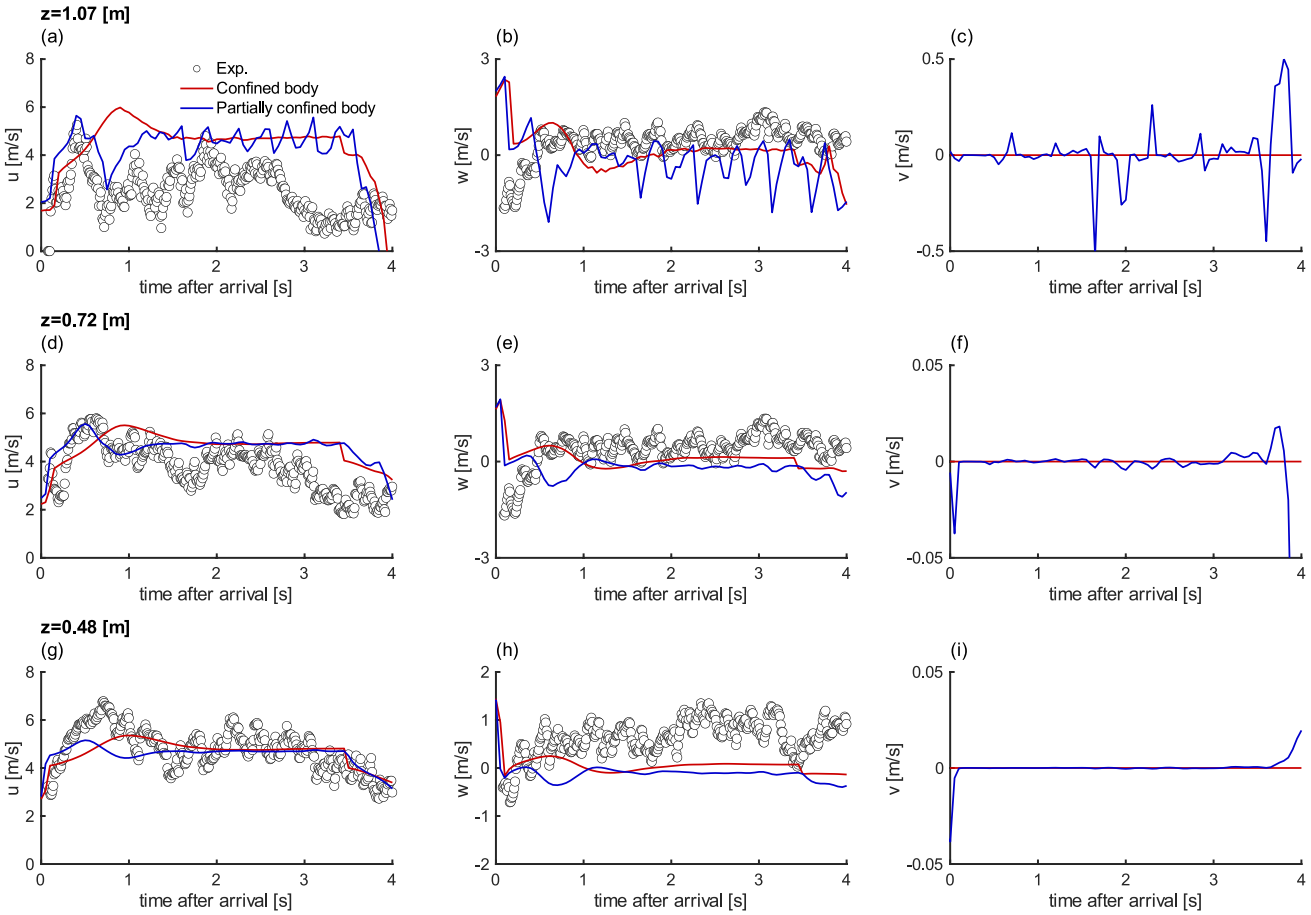

Fig. 9 **a**–**i** Comparisons of velocities at profile 2 at three different levels: $z = 0.48$, 0.72, and 1.07 m. u, v, and w represent the velocity components in the horizontal, perpendicular to the wall, and vertical directions, respectively. Black circles denote experimental results; red lines denote the confined condition; blue lines denote the partially confined condition. Under confined conditions, the values tend to stabilize and are generally close to the average of the observed values. The partially confined condition effectively reproduces temporal variations in the velocity field, with values at 0.72 and 1.07 m, notably aligning closely with the experimental results

overestimates the experimental body height by 0.3–1.0 m, while the partially confined condition reduces the error to about 0.2 m, except for a variation occurring between 0.5 and 1.0 s. This suggests that the reproduction of the horizontal velocity decrease is linked to the accuracy of height reproduction.

The simulated lateral velocities (Fig. 9c) showed that, as before, there is slight oscillation at relatively low depths, and the velocities are almost zero under both calculation conditions. However, the oscillations increased significantly near the height of the side wall, with a value of $z = 1.07$ m. In particular, the larger values near the wall suggest an active exchange of ambient air with the outside of the channel.

Temperature

Temperature change is also essential to understanding the behaviour of PDCs. We plotted sideviews of both simulations (Fig. 10a, b) and compared four points of experimental results in profile 2 (Fig. 10c, d). Because we used time- and depth-averaged values as boundary conditions, and only consider the temperature of the mixture in the simulations, a more detailed investigation of the modelling is required. This fact may have particularly affected the results in the lower flow region ($z = 0.725$ m). Although both conditions use time- and depth-averaged boundary conditions, the simulation results of temperature in confined and partially confined scenarios differ. Under confined conditions, the vortices, which are developed at the front and transported to the rear of the head, show a temperature decrease of about 2–4 K (Fig. 10a, 1.0–2.0 s). A similar temperature drop is observed on the surface of the body where the vortices form. This region corresponds to the observation point at $z = 1.08$ and 1.42 m, and the fluctuation has also been observed in the experimental results (Fig. 10c, z = 1.08, 1.42 m). In the body region, no significant temperature fluctuations are detected (Fig. 10a, 3.0–4.0 s). Eventually, the temperature decreases again as the tail passes (Fig. 10a, 5.0 s). As

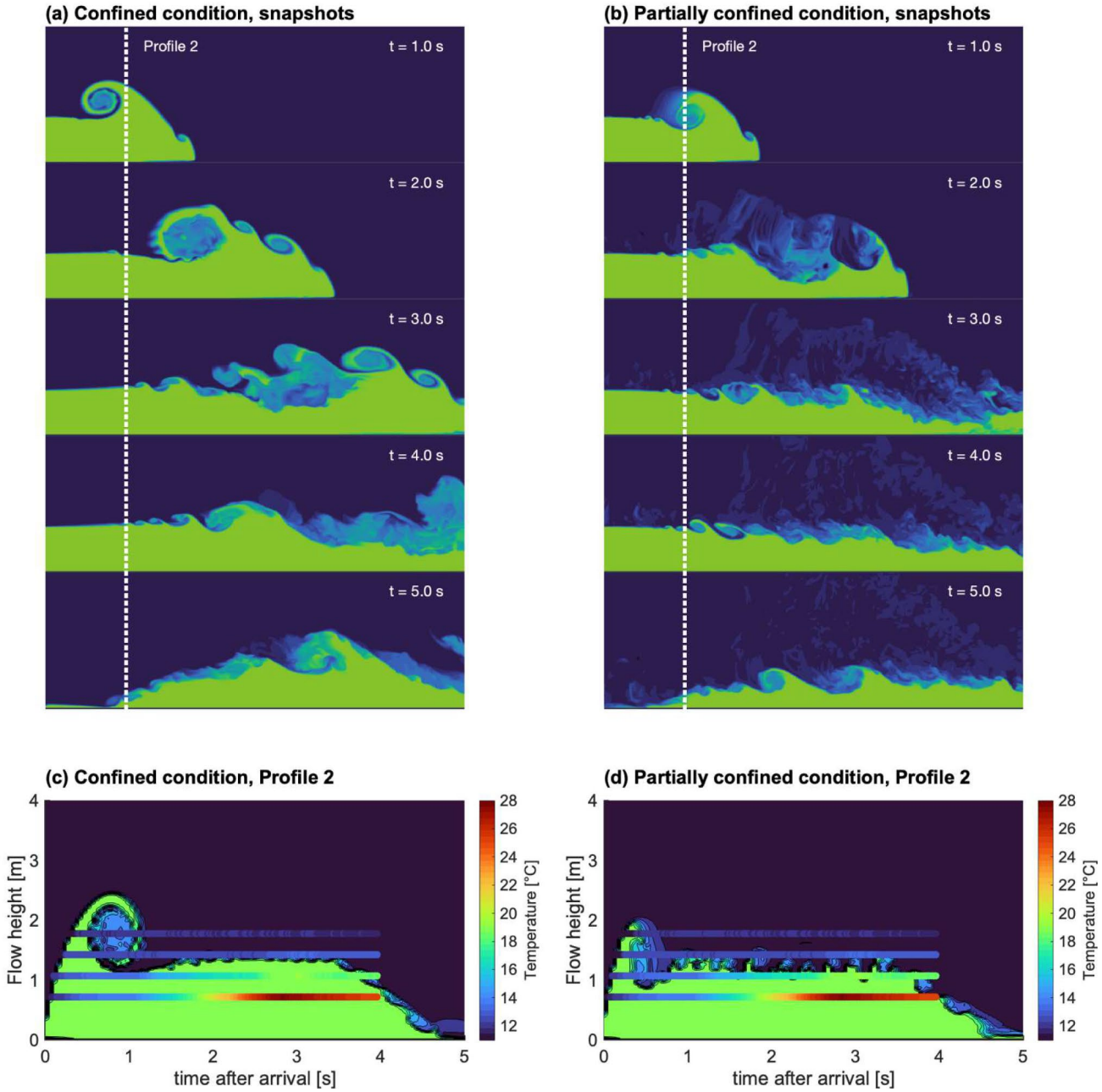

Fig. 10 **a**, **b** Sideview of temperature at the centre of flumes. Temperature distribution, similar to the volume fraction of particles, shows temperature drops in the regions behind the head where the vortices are developed, as well as on the surface of the body due to the mixing of ambient air. **c**, **d** Temperature at profile 2. Contours represent simulation results, and horizontal lines denote experimental data at $H = 0.72$, 1.08, 1.42, and 1.78 m. Partially confined conditions represent the temperature variations caused by turbulent fluctuations at $H = 1.0$–1.5 m

previously discussed, the development of the head, which reaches a height of 2.7 m, and the height of the body are influenced by the lateral boundary conditions. This also causes 4 K higher temperature in the head, and the calculation results differ from the experimental results (Fig. 10c). Besides, the partially confined condition causes a more rapid temperature drop than the confined condition due to mixing with the ambient fluid. In the same way that the concentration of particles decreases, the temperature at the surface of the body also decreases by 3–5 K (Fig. 10b, 3.0–5.0 s). Therefore, the partially confined condition reproduces the experimental results relatively better, including the temperature drop and a slight temperature increase in the latter part (Fig. 10d, z = 1.08, 1.42 m, $t = 3.0 \sim 4.0$ s). The partially

confined condition had an ambient temperature due to the transition to a more dilute wake behind the head, which is consistent with the experimental measurements. Due to the sufficiently low temperature, it is presumed that there are no large impacts on density variations. Nonetheless, future investigations are anticipated to explore whether particles or air control the temperature change in flows under transient depth-dependent input conditions, especially in the lower part of the body; where the particle–particle interactions are particularly prominent, it would be necessary to consider thermal nonequilibrium effects (Neri et al. 2003).

Entrainment

In previous experimental studies by Breard and Lube (2017) and Andrews (2014), the entrainment coefficient, E, is defined as $E = \frac{W}{U}$, U is streamwise velocity, and W is cross-stream velocity. This is based on the Morton-Turner-Taylor hypothesis and applied to many cases of gravity currents (Turner 1986). In this study, we determined the vertical velocity by taking the time derivative of wake and body height over the flow $W = d\bar{h}/dt$.

$$E = \frac{W}{U} = \frac{\frac{d\bar{h}}{dt}}{\frac{dx_N}{dt}} \tag{20}$$

The head velocity dx_N/dt is calculated from the depth-averaged value of the streamwise velocity at the head position. Under confined conditions, there is no clear difference between wake and body height (Fig. 11a, b). Until $t = 1.0$ s, the head keeps its size ($h_{body} \sim 2.0$ m), and the following part has the same height as the initial conditions. After t = 1.0 s, the mixing at the rear of the head has an impact. Therefore, the variations of the flow height at both the body and wake are almost the same (Fig. 11c). The increase in average flow height is greatest when the head grows, and the subsequent flows does not fully enter the channel (Fig. 11c, t = 0.5 s). Conversely, under partially confined conditions, examining the velocity calculated from height fluctuations reveals that both the body and wake regions exhibit an increase in thickness, particularly noticeable in the wake region, indicating significant entrainment (Fig. 11f). Until $t = 1.5$ s, average velocity calculated from the body and head height shows that the thickness of both regions is increasing at a rate of approximately 0.5 m/s or more. This observation suggests that while entrainment by vortices developed at the head determines flow height, accounting for three-dimensionality implies dilution progresses due to vortex collapse and flow around the sidewall edges. Furthermore, this would explain the previously mentioned computational results, where the temperature drop is 1–2 K greater than under the confined conditions. The mixing process caused by the entrainment might contribute to the decrease in temperature. Between $t = 1.5 \sim 2.0$ s, the difference in variation of flow height between the body and wake regions decreases once again, suggesting a transient modification in flow structure and potential suppression of vertical motion upon entering Sect. 3 (Fig. 11f).

Considering these changes in flow height and vertical velocities, we will examine the Richardson number Ri and the entrainment coefficient E in detail. The definition of Ri is consistent with that used in a previous study (Breard & Lube 2017).

$$Ri = \frac{(\rho_m - \rho_a) g\bar{h}}{\rho_a U^2} = \frac{\frac{\rho_m - \rho_a}{\rho_a} g\bar{h}}{\left(\frac{dx_N}{dt}\right)^2} \tag{21}$$

Entering Sect. 1, where the head is developing ($x_N \leq 1$), both the Ri and E show no differences between confined and partially confined conditions (Fig. 12a, b). This indicates that the sidewall height in Sect. 1 is sufficient, resulting in minor impacts in the lateral direction. Subsequently, under the confined condition, as the flow develops while maintaining higher density, buoyancy-induced energy consumption increases, leading to an increase Ri; however, in the calculation domain close to the inflow, Ri reached a maximum of 0.9 in Sect. 2, and although it gradually decreased thereafter, the turbulent component did not decay significantly. E exhibits notable development in Sect. 1 and reached the maximum value ($E = 0.2$). Although the flow height increased throughout the flows, eventually E reaches around 0.06. Under the partially confined conditions, considering the complexity of three-dimensional behaviour, Ri reached around 0.6. In parallel, E shows significant differences between the wake and body in Sect. 2. From Fig. 11, the increase in height in the body region is remarkable, whereas both increase and decrease are observed in the wake region. Consequently, the increase in height is smaller in the wake compared to the body when averaged over the entire flow. From later Sect. 2 ($x_N \geq 6.0$), and entering Sect. 3, further turbulence is generated, with the development of the wake region surpassing that of the body region. The entrainment coefficient showed $E = 0.2 \pm 0.02$, while Ri represented a value of 0.7 ± 0.1 in Sect. 2. These values align with those observed in the dilute PDCs provided by laboratory experiments (Andrews (2014); Breard & Lube (2017)). Generally, as the Ri increases, E decreases, with this tendency broadly confirmed in this study. Significantly, the sudden change around $x_N \sim 8.0$ m may indicate variations in turbulence components and entrainment rates.

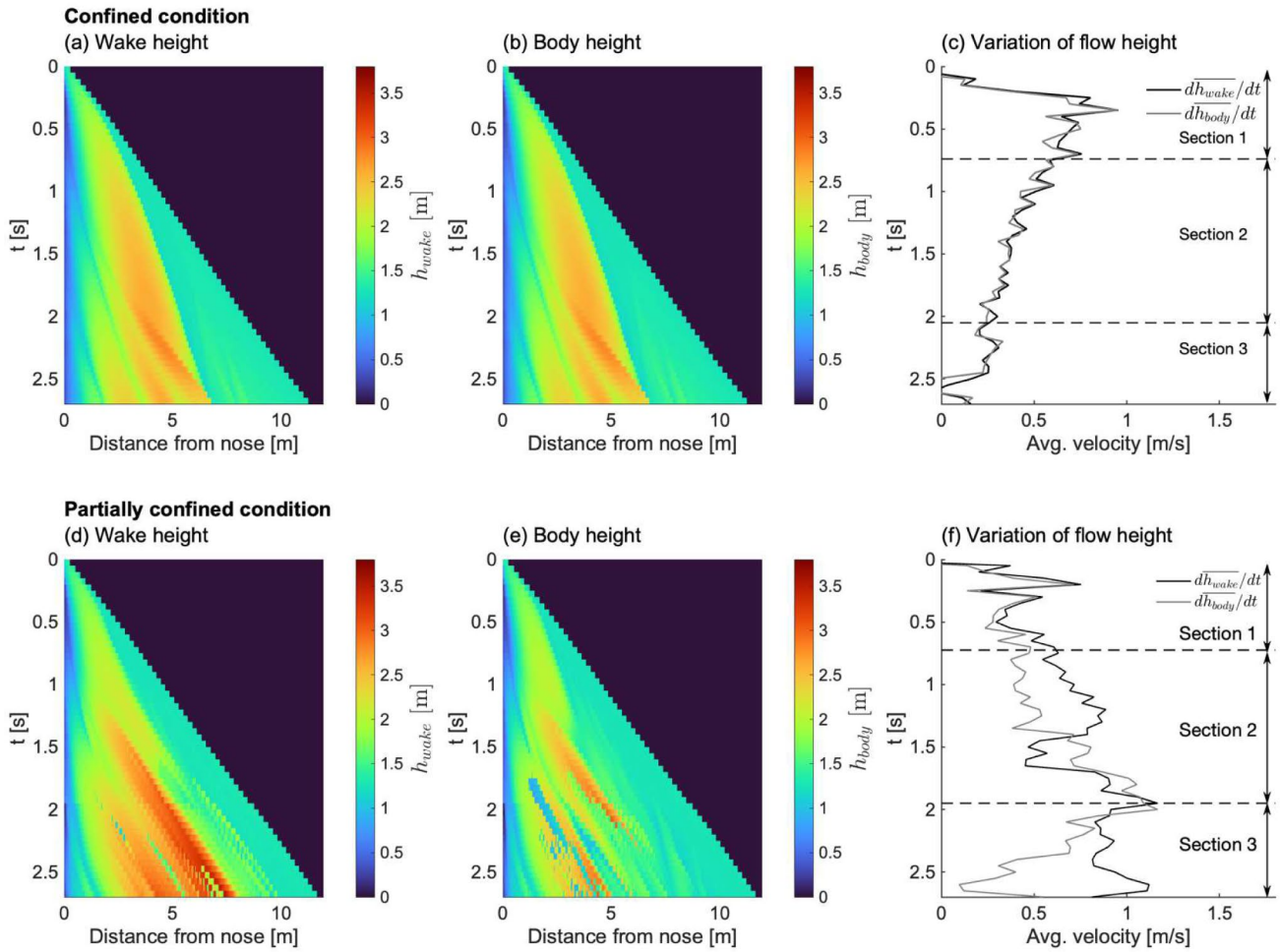

Fig. 11 Wake and body height, and differentials of each height under confined and partially confined conditions. From the height map, body and wake heights are generally consistent under confined conditions (**a**, **b**); whereas under partially confined conditions, there is a clear difference between wake and body height under partially confined conditions (**d**, **e**). **c**, **f** Vertical velocity component based on height variations. In confined conditions, the variations are comparable (**c**); however, in partially confined conditions, distinct differences arise between wake and body (**f** $t = 0.5 \sim 1.5$ s, $2.0 \sim 2.5$ s)

Conclusion

We have compared the results of a large-scale experiment at the PELE facility which was solved with a three-dimensional LES mixture model, considering confined and partially confined conditions. It was possible to obtain results in rough agreement with the experimental results, even if the calculations were performed under confined conditions, near the two-dimensional condition, without considering the actual channel walls used in the experiments. In particular, the comparison of flow heights showed much closer values for the confined condition than the results for the partially confined condition. On the other hand, there is an apparent lateral overspill and mass loss toward lateral directions under partially confined conditions. The amount of confinement significantly influences the velocity variation of the flow, especially the velocity structure inside the flow. The calculated velocities in the x- and z-direction under the partially

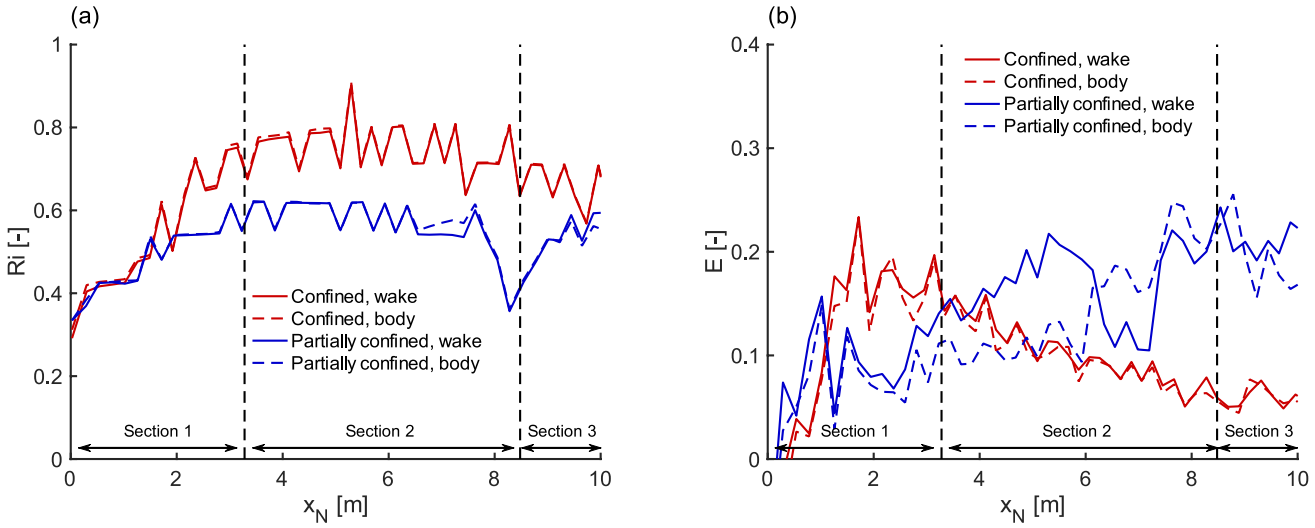

Fig. 12 **a** Richardson number and **b** entrainment coefficient. Solid and dashed lines denoted entrainment coefficient at wake and body, respectively. Red lines denoted the confined condition; blue lines denoted the partially confined condition. Black dot lines represented each section. Due to the limitation of lateral flows, the confined conditions represent small entrainment; however, the partially confined results indicate the entrainment rate at wake region is 0.2 ± 0.02 and body region is 0.15 ± 0.02, respectively. In particular, this difference becomes distinctly evident after the nose enters the mid-sections

confined condition reproduce the tendency for higher points to exhibit larger fluctuations of velocities. The maximum or average values also show close values. In contrast, the calculated velocities in the lateral direction, which cannot be considered in the two-dimensional model, are significantly different near the wall and in the centre, suggesting that active lateral interactions are likely to result in flow conditions close to the experimental data.

The LES model used in this study performed well in pyroclastic flow calculations. The head shape was clear in both profiles, and the body heights matched reasonably well with filter widths such as those conventionally used in gravity flow calculations. Simplifications such as the turbulence model (LES), a sufficiently homogeneous state of PDC, and input conditions averaged in time and space may lead to an overestimation of the wake height and lateral outflow. Therefore, future research should involve examining turbulence models, including the treatment of turbulent diffusion terms using density differences, as well as detailed modelling of sedimentation processes, such as particle interactions and settling effects. Detailed comparisons with models that focus on different physical processes developed to date are also expected. Andrews (2014) has proposed a process in which the heated flow rises upward while suppressing lateral dispersion, with the entrainment process transitioning between the head and tail of the flow. Further investigation is needed to account for temperature and density differences to understand the entrainment process in PDC.

Finally, compressibility was not extremely important under the conditions covered in this study, as the effects of temperature and pressure changes were smaller than in natural volcanic events. In the studies of outgoing flow caused by the impact of ash column collapse, Valentine and Sweeney have investigated how the concentration of particles and particle size affect the behaviour of the outgoing compressible flow (e.g. Sweeny & Valentine (2017), Valentine & Sweeney (2018), Valentine (2020)). Hence, it is necessary to confirm whether the proposed model can be applied to compressible turbulence using future observational data from actual PDCs.

Supplementary Information The online version contains supplementary material available at https://doi.org/10.1007/s00445-025-01799-z.

Acknowledgements This manuscript was improved by the comments from Editor Prof. Greg Valentine and two anonymous reviewers. We express great gratitude to Dr. Ermano Brosch and Dr. Matteo Cerminara for sharing the experimental dataset in this study. Dr. Shimizu A Hiroyuki and Prof. Andrew W. Woods gave valuable comments in the early stages of this study.

Author contribution ST contributed to this study's conception and design. GL prepared experimental datasets. ST and TN developed the numerical code. ST and GL performed numerical simulations and analyses. ST wrote the first draft of the manuscript and all authors commented on the previous versions of the manuscript.

Funding This work was supported by the funding of JSPS KAKENHI Grant Number 22J23301.

Data availability Not applicable.

Code availability The numerical codes used to generate the results are available upon request from the corresponding author.

Declarations

Conflict of interest The authors declare no competing interests.

References

Andrews BJ (2014) Dispersal and air entrainment in unconfined dilute pyroclastic density currents. Bull Volcanol 76:1–14. https://doi.org/10.1007/s00445-014-0852-4

Andrews BJ, Manga M (2011) Effects of topography on pyroclastic density current run-out and formation of coignimbrites. Geology 39:1099–1102. https://doi.org/10.1130/G32226.1

Andrews BJ (2019) Recognizing unsteadiness in the transport systems of dilute pyroclastic density currents. Bull Volcanol 81. https://doi.org/10.1007/s00445-018-1266-5

Ashurst WT, Meiburg E (1988) Three-dimensional shear layers via vortex dynamics. J Fluid Mech 189:87–116

Auker MR, Sparks RSJ, Siebert L, Crossweller H, Ewert J (2013) A statistical analysis of the global historical volcanic fatalities record. J Appl Volcanol 2:. https://doi.org/10.1186/2191-5040-2-2

Baxter PJ, Jenkins S, Seswandhana R, Komorowski JC, Dunne K, Purser D, Voight B, Shelley I (2017) Human survival in volcanic eruptions: thermal injuries in pyroclastic surges, their causes, prognosis and emergency management. Burns 43:1051–1069. https://doi.org/10.1016/j.burns.2017.01.025

Bini M, Jones WP (2008) Large-eddy simulation of particle-laden turbulent flows. J Fluid Mech 614:207–252

Breard ECP, Lube G (2017) Inside pyroclastic density currents–uncovering the enigmatic flow structure and transport behaviour in large-scale experiments. Earth Planet Sci Lett 458:22–36. https://doi.org/10.1016/j.epsl.2016.10.016

Breard E, Dufek J, Roche O (2019a) Continuum modeling of pressure-balanced and fluidized granular flows in 2-D: comparison with glass bead experiments and implications for concentrated pyroclastic density currents. J Geophys Res Solid Earth 124:5557–5583. https://doi.org/10.1016/0022-0396(87)90038-6

Breard EC, Jones JR, Fullard L, Lube G, Davies C, Dufek J (2019b) The permeability of volcanic mixtures—implications for pyroclastic currents. J Geophys Res Solid Earth 124(2):1343–1360

Brosch E, Lube G (2020) Spatiotemporal sediment transport and deposition processes in experimental dilute pyroclastic density currents. J Volcanol Geoth Res 401:106946

Caulfield CP, Peltier WR (1994) Three dimensionalization of the stratified mixing layer. Phys Fluids 6(12):3803–3805

Caulfield CP, Yoshida S, Peltier WR (1996) Secondary instability and three-dimensionalization in a laboratory accelerating shear layer with varying density differences. Dyn Atmos Oceans 23(1–4):125–138

Cerminara M, Esposti Ongaro T, Neri A (2016) Large eddy simulation of gas–particle kinematic de-coupling and turbulent entrainment in volcanic plumes. J Volcanol Geoth Res 326:143–171. https://doi.org/10.1016/j.jvolgeores.2016.06.018

Cerminara M, Brosch E, Lube G (2021) A theoretical framework and the experimental dataset for benchmarking numerical models of dilute pyro-clastic density currents. arXiv preprint http://arxiv.org/abs/2106.14057

Charbonnier SJ, Gertisser R (2008) Field observations and surface characteristics of pristine block-and-ash flow deposits from the 2006 eruption of Merapi Volcano, Java, Indonesia. J Volcanol Geoth Res 177(4):971–982

Chedeville C, Roche O (2014) Autofluidization of pyroclastic flows propagating on rough substrates as shown by laboratory experiments. J Geophys Res Solid Earth 119(3):1764–1776

Chedeville C, Roche O (2015) Influence of slope angle on pore pressure generation and kinematics of pyroclastic flows: insights from laboratory experiments. Bull Volcanol 77:1–13

Deardorff JW (1970) A numerical study of three-dimensional turbulent channel flow at large Reynolds numbers. J Fluid Mech 41(2):453–480

Dellino P, Büttner R, Dioguardi F, Doronzo D, Volpe LL, Mele D, Sonder I, Sulpizio R, Zimanowski B (2010b) Experimental evidence links volcanic particle characteristics to pyroclastic flow hazard. Earth Planet Sci Lett 295:314–320. https://doi.org/10.1016/j.epsl.2010.04.022

Dellino P, Dioguardi F, Doronzo DM, Mele D (2019) The rate of sedimentation from turbulent suspension: an experimental model with application to pyroclastic density currents and discussion on the grain-size dependence of flow run-out. Sedimentology 66(1):129–145

Dellino P, Dioguardi F, Doronzo DM, Mele D (2020) A discriminatory diagram of massive versus stratified deposits based on the sedimentation and bedload transportation rates. Experimental investigation and application to pyroclastic density currents. Sedimentology 67(4):2013–2039

Dellino P, Dioguardi F, Rinaldi A, Sulpizio R, Mele D (2021) Inverting sediment bedforms for evaluating the hazard of dilute pyroclastic density currents in the field. Sci Rep 11(1):21024

Dellino P, Zimanowski B, Büttner R, Volpe LL, Mele D, Sulpizio R (2007) Large-scale experiments on the mechanics of pyroclastic flows: design, engineering, and first results. J Geophys Res Solid Earth 112:. https://doi.org/10.1029/2006JB004313

Dellino P, Dioguardi F, Zimanowski B, Büttner R, Mele D, La Volpe L, Sulpizio R, Doronzo DM, Sonder I, Bonasia R, Calvari S, Marotta E (2010a) Conduit flow experiments help constraining the regime of explosive eruptions. J Geophys Res Solid Earth 115(B4).

Esposti Ongaro T, Cerminara M, Charbonnier SJ, Lube G, Valentine GA (2020) A framework for validation and benchmarking of pyroclastic current models. Bull Volcanol 82:1–17

Esposti Ongaro T, Barsotti S, Neri A, Salvetti MV (2011) Large-eddy simulation of pyroclastic density currents. In: ERCOFTAC Series. Springer Netherland, pp 161–170

Fujinawa A, Ban M, Ohba T, Kontani K, Miura K (2008) Characterisation of low-temperature pyroclastic surges that occurred in the northeastern Japan arc during the late 19th century. J Volcanol Geoth Res 178:113–130. https://doi.org/10.1016/j.jvolgeores.2008.07.00

Germano M, Piomelli U, Moin P, Cabot WH (1991) A dynamic subgrid-scale eddy viscosity model. Phys Fluids A 3(7):1760–1765

Girolami L, Roche O, Druitt TH, Corpetti T (2010) Particle velocity fields and depositional processes in laboratory ash flows, with implications for the sedimentation of dense pyroclastic flows. Bull Volcanol 72:747–759

Gueugneau V, Charbonnier S, Roche O (2022) PyroCLAST: a new experimental framework to investigate overspilling of channelized, concentrated pyroclastic currents. Bull Volcanol 85(1):5

Gueugneau V, Charbonnier S, Esposti Ongaro T, de'Michieli Vittuti M, Peruzzetto M, Mangeney A, Bouchut F, Patra A, Kelfoun K (2021) Synthetic benchmarking of concentrated pyroclastic current models. Bulletin of Volcanology 83:. https://doi.org/10.1007/s00445-021-01491-y

Harlow FH, Welch JE (1965) Numerical calculation of time-dependent viscous incompressible flow of fluid with free surface. Phys Fluids 8(12):2182

Ishimine Y (2005) Numerical study of pyroclastic surges. J Volcanol Geoth Res 139:33–57. https://doi.org/10.1016/j.jvolgeores.2004.06.017

Kieffer SW (1984) Factors governing the structure of volcanic jets. Explos Volcanism Inception Evol Hazards 11:143–157

Klaassen GP, Peltier WR (1985) The onset of turbulence in finite-amplitude Kelvin-Helmholtz billows. J Fluid Mech 155:1–35
Klaassen GP, Peltier WR (1991) The influence of stratification on secondary instability in free shear layers. J Fluid Mech 227:71–106
Kunii D, Levenspiel O (1969) Fluidization engineering. John Wiley, New York
Lube G, Breard ECP, Cronin SJ, Jones J (2015) Synthesising large-scale pyroclastic flows: experimental design, scaling, and first results from PELE. J Geophys Res Solid Earth 120:1487–1502. https://doi.org/10.1002/2014JB011666
Lube G, Breard ECP, Esposti-Ongaro T, Dufek J, Brand B (2020) Multiphase flow behaviour and hazard prediction of pyroclastic density currents. Nat Rev Earth Environ 1:348–365
Lube G, Cronin SJ, Thouret JC, Surono K (2011) Kinematic characteristics of pyroclastic density currents at Merapi and controls on their avulsion from natural and engineered channels. Bulletin 123(5–6):1127–1140.
Martin JE, Meiburg E (1991) Numerical investigation of three-dimensionally evolving jets subject to axisymmetric and azimuthal perturbations. J Fluid Mech 230:271–318
Mason PJ, Callen NS (1986) On the magnitude of the subgrid-scale eddy coefficient in large-eddy simulations of turbulent channel flow. J Fluid Mech 162:439–462
Neri A, Esposti Ongaro T, Macedonio G, Gidaspow D (2003) Multiparticle simulation of collapsing volcanic columns and pyroclastic flow. J Geophys Res Solid Earth 108. https://doi.org/10.1029/2001jb000508
Roche O, Montserrat S, Niño Y, Tamburrino A (2010) Pore fluid pressure and internal kinematics of gravitational laboratory air-particle flows: insights into the emplacement dynamics of pyroclastic flows. J Geophys Res Solid Earth 115(B9).
Salehipour H, Caulfield CP, Peltier WR (2016) Turbulent mixing due to the Holmboe wave instability at high Reynolds number. J Fluid Mech 803:591–621
Shen L, Yue DK (2001) Large-eddy simulation of free-surface turbulence. J Fluid Mech 440:75–116
Shimizu HA, Koyaguchi T, Suzuki YJ, Brosch E, Lube G, Cerminara M (2021) Validation of a two-layer depth-averaged model by comparison with an experimental dilute stratified pyroclastic density current. Bulletin of Volcanology 83:. https://doi.org/10.1007/s00445-021-01493-w
Smagorinsky J (1963) General circulation experiments with the primitive equations: I The Basic Experiment. Mon Wea Rev 91(3):99–164
Smyth WD (2006) Secondary circulations in Holmboe waves. Phys Fluids 18(6).
Sparks RSJ, Wilson L, Hulme G (1978) Theoretical modeling of the generation, movement, and emplacement of pyroclastic flows by column collapse. J Geophys Res Solid Earth 83(B4):1727–1739
Sweeney MR, Valentine GA (2017) Impact zone dynamics of dilute mono-and polydisperse jets and their implications for the initial conditions of pyroclastic density currents. Phys Fluids 29(9).
Thorpe SA (1971) Experiments on the instability of stratified shear flows: miscible fluids. J Fluid Mech 46(2):299–319
Thorpe SA (1987) Transitional phenomena and the development of turbulence in stratified fluids: a review. J Geophys Rese Oceans 92(C5):5231–5248
Turner JS (1986) Turbulent entrainment: the development of the entrainment assumption, and its application to geophysical flows. J Fluid Mech 173:431–471. https://doi.org/10.1017/S0022112086001222
Valentine GA (2020) Initiation of dilute and concentrated pyroclastic currents from collapsing mixtures and origin of their proximal deposits. Bull Volcanol 82(2):20
Valentine GA, Sweeney MR (2018) Compressible flow phenomena at inception of lateral density currents fed by collapsing gas-particle mixtures. J Geophys Res Solid Earth 123(2):1286–1302
Van Driest ER (1956) On turbulent flow near a wall. J Aeronautical Sci 23(11):1007–1011
Weit A, Roche O, Dubois T, Manga M (2018) Experimental measurement of the solid particle concentration in geophysical turbulent gas-particle mixtures. J Geophys Res Solid Earth 123(5):3747–3761
Welch JE, Harlow FH, Shannon JP, Daly BJ (1965) The MAC method-a computing technique for solving viscous, incompressible, transient fluid-flow problems involving free surfaces (No. LA-3425). Los Alamos National Lab.(LANL), Los Alamos, NM (United States).
Yabe T, Wang PY (1991) Unified numerical procedure for compressible and incompressible fluid. J Phys Soc Japan 60:2105–2108. https://doi.org/10.1143/JPSJ.60.2105
Yabe T, Mizoe H, Takizawa K, Moriki H, Im HN, Ogata Y (2004) Higher-order schemes with CIP method and adaptive Soroban grid towards mesh-free scheme. J Comput Phys 194(1):57–77

Springer Nature or its licensor (e.g. a society or other partner) holds exclusive rights to this article under a publishing agreement with the author(s) or other rightsholder(s); author self-archiving of the accepted manuscript version of this article is solely governed by the terms of such publishing agreement and applicable law.